THESIS

SURFACE HEAT FLUXES AND MJO PROPAGATION THROUGH THE MARITIME CONTINENT

Submitted by

Justin Hudson

Department of Atmospheric Science

In partial fulfillment of the requirements

For the Degree of Master of Science

Colorado State University

Fort Collins, Colorado

Spring 2022

Master's Committee:

Advisor: Eric Maloney

Kristen Rasmussen
Jeremy Rugenstein

ABSTRACT

SURFACE HEAT FLUXES AND MJO PROPAGATION THROUGH THE MARITIME CONTINENT

The 'barrier effect' of the Maritime Continent (MC) is a known hurdle in understanding the propagation of the Madden-Julian Oscillation (MJO). To understand the differing dynamics of MJO events that propagate versus stall over the MC, a new MJO tracking algorithm utilizing 30-96 day filtered NOAA Interpolated OLR anomalies is presented. Using this algorithm, MJO events can be identified, tracked, and described in terms of their propagation characteristics. Latent heat flux from CYGNSS and OAFLUX as well as CYGNSS surface winds are used to compare large-scale patterns for MJO events that do and do not propagate through the MC. Local area-averaged surface fluxes and OLR anomalies are 7-14% and 18-22% of the value of precipitation anomalies, respectively. While differences in these contributions do not change substantially for propagating versus terminating events, precipitation events that successfully propagate through the MC demonstrate surface flux anomalies that are stronger and more spatially-coherent.The spatial scale of precipitation events that propagate through the MC region is also larger than terminating events. It is also shown that large-scale enhancement of latent heat fluxes near and to the east of the Dateline accompanies MJO events that successfully propagate through the MC.This large-scale enhancement of latent heat fluxes to the east of the Dateline is equally driven by dynamic and thermodynamic effects. These findings are placed in the context of recent theoretical models of the MJO in which latent heat fluxes are important for propagation and destabilization. The tracking algorithm is also used to show for historical and greenhouse gas warming scenarios in CESM2 that MJO propagation speed increases and precipitation anomalies propagate further east with warming. However, the CESM2 inadequately represents the 'barrier effect' of the MC region on propagating MJO events.

ACKNOWLEDGMENTS

This work was supported by NASA CYGNSS grant 80NSSC21K1004 and NOAA CVP grant NA18OAR4310299.

TABLE OF CONTENTS

1 Introduction

The Madden Julian Oscillation (MJO; Madden and Julian, 1971; 1972) is a tropical intraseasonal (30-90 day) oscillation, maximizing in amplitude in boreal winter, which propagates eastward along the equator. The classical picture of the MJO is that of a large-scale enhanced precipitation region zonally bound by suppressed precipitation that propagates from the Indian Ocean (IO), through the Maritime Continent (MC), and then into the Pacific Ocean where it dissipates. The spatial scale of the MJO precipitation envelope is of zonal wavenumber 1-3 (Wheeler and Kiladis, 1999). The MJO is also coupled to a large-scale anomalous circulation which spans much of the tropics (e.g. Maloney and Hartmann 2000b).

The influence of the MJO extends beyond the Indo-Pacific Warm Pool, with MJO teleconnections impacting regions across the globe (Arcodia et al., 2020; Barnes et al., 2019; Lee and Seo, 2019; Zhou et al., 2012). For example, the MJO produces Rossby wave teleconnections to the extratropics that impact atmospheric river activity along the West Coast of the United States (e.g. Guan and Waliser, 2015). The boreal summer counterpart of the MJO, sometimes called the Boreal Summer IntraSeasonal Oscillation (BSISO), also produces teleconnections to the Western Hemisphere that modulate tropical cyclones in the east Pacific and Atlantic (Maloney and Hartmann, 2000a,b). Rossby waves produced by the MJO also modulate polar sea ice loss and recovery through anomalous heat transport (e.g. Lee and Seo, 2019), and anomalous wind driven ocean circulation produced by the MJO can possibly impact the tilt of the Earth (Afroosa et al., 2021).

These global teleconnections also mean the MJO plays an important role in forecasting skill on subseasonal to seasonal timescales (S2S; Baggett et al., 2017; Nardi et al., 2020). The inability of forecasting models to properly simulate MJO propagation across the MC has negative implications for S2S forecast skill in western North America and other regions (e.g. Hsiao et al., 2022, submitted). Inability of climate models to simulate the MJO has potentially important implications for simulation of lower frequency tropical variability such as that associated with the El Niño-Southern Oscillation, as wind bursts associated with MJO events can initiate El Niño activity (e.g. McPhaden 1999).

Despite the importance of the MJO for climate, extreme events, and subseasonal prediction, there are many unanswered questions about its formation, maintenance, and propagation (Jiang et al., 2020; Zhang, 2005). One mystery surrounding the MJO is known as the 'barrier effect' of the MC (Salby and Hendon, 1994; Zhang and Ling, 2017). A sizable fraction of MJO events fail to propagate through or weaken over the MC region (Ling et al., 2019). Those that do make their way through the MC region tend to detour south of the island of Java (Wu and Hsu, 2009). The MC tends to produce too much of a barrier to

MJO propagation in many global models (Inness and Slingo, 2006), which negatively affects the ability of models to predict the MJO (e.g. Kim et al., 2014). A variety of processes are hypothesized to affect MJO propagation across the MC, including a prior strong dry anomaly in the west Pacific (Kim et al., 2014), the diurnal cycle over MC islands (Zhang and Ling, 2017), westward propagating Rossby waves in the west Pacific (DeMott et al., 2018), air-sea coupling (Hirata et al., 2013), and competing westward propagating intraseasonal modes (e.g. Gonzalez and Jiang, 2019). Jing et al. (2020) provides an extensive summary of many of these hypothesized processes. Recent studies with CMIP6 models suggest that MJO propagation through the MC may be improved in the most recent generation of climate models (e.g. Ahn et al., 2020), a result they attribute to improved mean state horizontal moisture gradients in the MC region and their impact on horizontal moisture advection.

This paper will explore the possibility that surface flux variability helps to maintain MJO propagation through the MC. Variations in surface fluxes, latent heat flux (LHF) in particular, are believed to play a critical role in maintaining the MJO and guiding its propagation but the exact mechanism for how LHF supports the MJO and how much it does it still a matter of debate (Bui et al., 2020; DeMott et al., 2014; DeMott et al., 2015; Emanuel, 2020; Fuchs and Raymond, 2017; Khairoutdinov and Emanuel, 2018; Maloney, 2009; Raymond and Fuchs, 2018; Riley Dellaripa and Maloney, 2015; Sentić et al., 2020; Sobel and Maloney, 2012; Wolding and Maloney, 2015).

Two major recent bodies of theory suggest the importance of wind-induced surface fluxes for MJO maintenance and propagation, and will guide the investigations here. The first is moisture mode theory (e.g. Sobel and Maloney, 2012,2013; Adames and Kim, 2016). Assuming weak tropical temperature gradients, moisture mode theory argues that processes regulating the evolution of the tropical moisture field, which then modulates precipitation, are essential to the dynamics of the MJO. Some studies have argued that cloud radiative feedbacks onto the moisture budget, where longwave radiative perturbations are of magnitude 20% of MJO precipitation anomalies, help to maintain MJO convection. Other studies have argued that surface flux feedbacks, largely wind-driven, can also support MJO moisture anomalies that support convection (Araligidad and Maloney, 2008; Bui et al., 2020). We hypothesize that surface flux anomalies help to support MJO convective events that propagate through the MC. A key aspect of this investigation is the strength of MJO LHF anomalies relative to precipitation anomalies in the MC region, especially when compared to the strength of OLR anomalies versus precipitation, as radiative feedbacks have previously been shown to help maintain MJO convection (Adames and Kim, 2016).

Another body of theory of referred to as Wind-Induced Surface Heat Exchange (WISHE), argues that enhanced surface fluxes to the east of MJO convection help to support eastward MJO propagation in the presence of mean tropical easterly low-level winds (Emanuel, 1987; Raymond and Fuchs 2018; Sentić et al., 2020). We hypothesize that MJO events that propagate across the MC are associated with a stronger enhanced LHF signal in the central and eastern Pacific than non-propagating events. Both groups of theory place LHF as a key underpinning to how the MJO maintains itself; to this end moisture mode theory relies on surface fluxes working in tandem with radiative feedbacks and horizontal moisture advection to enhance moist static energy (MSE) ahead of the MJO in contrast to the singular importance WISHE places on wind-driven fluxes east of the MJO for controlling propagation. Understanding what role LHF plays in controlling MJO propagation is a critical step towards a complete theory of the MJO.

Some studies to address MJO propagation through the MC have involved the use of indices based on empirical orthogonal function (EOF) analysis. Attempts to understand and predict the MJO using indices such as the Real-time Multivariate MJO Index (RMM; Wheeler and Hendon, 2004) and the Outgoing Longwave Radiation (OLR) based MJO Index (OMI; Kiladis et al., 2014) have involved breaking the MJO down into 8 phases based on the broad geographic location of the MJO's enhanced convective phase. Earlier phases place the MJO over the Indian Ocean, later phases over the Pacific Ocean. While these indices have allowed for greater insight into MJO dynamics they limit our understanding of exactly where the MJO's enhanced convective region is at any given time. For example, the RMM index is based on the leading two combined EOFs of OLR as well as upper and lower tropospheric winds, and provides only a broad indication of the location of enhanced MJO convection, or can provide a misleading indication of the presence of MJO convection given that wind anomalies most strongly determine the behavior of the index (e.g. Straub, 2013).

A more recent approach to understanding MJO propagation relies on using tracking algorithms to identify and track the MJO, this technique allows for better localization of the MJO convective center. Precipitation tracking has been shown to identify and locate MJO events providing information about MJO propagation as well as the MC 'barrier effect' (Kerns and Chen, 2016, 2020; Ling et al., 2017; Zhang and Ling., 2017). Kerns and Chen (2016, 2020) uses spatially smoothed 72-hour accumulated precipitation to track large scale ($>$300,000 km^2) anomalies, and found that the RMM index did not always agree with their tracking on the presence of an MJO event by either lacking an MJO signal during a period where they tracked a precipitation event, or producing a signal when there was no identified MJO event.

Singh and Kinter (2020) showed that intraseasonally filtered OLR anomalies combined with a multiple object tracking algorithm is capable of identifying, and tracking several classes of tropical intraseasonal oscillations. For example, they found that certain indices (e.g. RMM) do not accurate portray the behavior of the BSISO. Both Kerns and Chen (2016, 2020) and Singh and Kinter (2020) showed that direct identification and tracking methods are capable of highlighting key regional and global features for different categories of MJO events such as the relationship to the state of the El Niño Southern Oscillation (ENSO; Kerns and Chen 2016, 2020), and how seasonality of moisture, low-level circulation, and sea surface temperature (SST) control MJO propagation (Singh and Kinter, 2020).

Here, we develop a tracking technique that is inspired by that of Singh and Kinter (2020), and use it to understand the role of surface heat flux anomalies for MJO propagation through the MC region. Filtered OLR anomalies allow for a robust and coherent MJO identification technique for tracking, which can be used to diagnose the importance of surface flux feedbacks to MJO dynamics in the MC, and help explain why some events propagate through the MC, and others terminate. In section 2 we outline the specifics of our algorithm, as well as the data used to investigate the dynamics of MJO propagation and maintenance. In section 3, our method is used to assess the importance of surface flux feedbacks to MJO maintenance and propagation through the MC region, in the context of moisture mode and WISHE theory. In section 4 we apply our tracking algorithm to CESM2 experiments to examine how MJO propagation may change in a warming climate. In section 5 we discuss our results in the context of current theories of MJO propagation, and in section 6 we present our conclusions.

2 Methodology and Data

2.1 OLR Tracking Algorithm:

Interpolated daily mean OLR data on a 2.5° by 2.5° grid provided by NOAA/OAR/ESRL PSL, Boulder Colorado, USA, from their website (https://psl.noaa.gov/data/gridded/data.interp_OLR.html) from 1985-2019 (Liebmann and Smith, 1996) were used to diagnose the location of convection. To do this, the 30-year daily mean OLR (1981-2010) provided alongside the interpolated OLR data was subtracted grid-wise producing daily anomalies relative to the 30-year mean. The calculated anomalies were then filtered to isolate MJO timescale signals using a 30-96 day bandpass filter with a Hanning window. The OLR data was subsetted to the Indo-Pacific Warm Pool Region (20N-20S, 30-240E) where the MJO shows its strongest convective variability during boreal winter.

To highlight regions of enhanced intraseasonal convection, binary maps were produced whereby grid cells of filtered OLR anomalies less than -15 W/m^2 (similar to that of Singh and Kinter, 2020), indicating strong convection, were given a value of 1 and all other grid cells were given a value of zero. Our results are not qualitatively sensitive to varying this threshold between -10 to -20 W/m^2. These binary maps allow for an easily searchable space where regions of intraseasonal convection can be quickly identified.

The tracking algorithm works by first searching the produced binary maps for areas of enhanced convection. The algorithm then utilizes 8-connectivity (the fact that any point in 2D space has 8 neighboring points in the cardinal directions and their combinations) to map these regions out, and we refer to these mapped out regions henceforth as 'blobs.' Because the MJO convection anomalies have a large spatial scale (Wheeler and Kiladis, 1999), tracking was limited to blobs above a certain size threshold of 10 pixels (62.5 deg^2 on a 2.5° by 2.5° grid, or 750,000 km^2). Sensitivity to this threshold is low between 5-15 pixels, and then strongly increases outside of these bounds. Only blobs above this size threshold are tracked, if a blob falls below this threshold the tracked event is considered to have dissipated. Details on how we handle blobs that temporarily fall below this threshold are described later in this section.

From theory and observations we know that relative to its spatial scale, the MJO propagation speed is quite small (Madden and Julian, 1972; Adames and Kim, 2016). Leveraging this fact, once the algorithm has identified all the blobs on frame N (where 1 frame is equivalent to 1 day for the NOAA interpolated daily OLR) it then compares the grid points within each tracked blob against the grid points of blobs on frame N-1. Using the points within blobs on frames N and N-1, the two blobs can be connected using a blob similarity threshold where the sum of grid points in blob N that are found in blob N-1 are divided by the number of grid points in blob N (set to a value of 0.2, or 20% of points must be similar). This is different from the approach of Singh and Kinter (2020) who used a Kalman Filter to predict the location of a tracked event on a subsequent frame and searched in a specified radius around the predicted location. Because for the sake of completeness one already needs to search most, if not all, of the binary map for blobs, by eliminating this predictive step we potentially reduce the computational cost. This overlapping points methodology was used by Kerns and Chen (2016, 2020), although their threshold was set to 50% of points overlapping. We found that our results are not sensitive to this value unless set to very low or very high values. This process is repeated for all frames from October 1st, 1985 to May 31st, 2019 and is agnostic to where blobs originate, dissipate, and the direction and speed of their propagation. This minimizes issues such as when the center of convection temporarily stalls or moves westward on an individual day.

Previous tracking studies have shown that the path of individual MJO events, while generally moving eastward, can be complicated and that for a tracking algorithm to be robust it must account for tracked regions that overlap or split into multiple regions (Kerns and Chen, 2016; Singh and Kinter, 2020). To handle such variability our algorithm loops over the list of all tracked blobs to connect any events that may have been disrupted, temporarily fallen below a size or convective threshold, and other complex behavior. To accomplish this our algorithm draws a 50 degree wide (25 degrees to the East and West) and 15 degree tall (7.5 degrees to the North and South) box around the last known geometric centroid for a blob. If there is another tracked blob in that box within 10 frames of when the blob dissipated, which persists for at least 10 days, the algorithm considers the two events to be connected and combines them into a singular event. If there are multiple blobs the algorithm chooses the largest blob and declares that as the continuation of the original blob. During our sensitivity testing, when the length of time connecting blobs persist is reduced, events that drastically change direction and propagate from the Pacific Ocean or the MC into the Indian Ocean begin to appear. By limiting the connection of blobs to those blobs that last for several days the change for MJO events to be connected to spurious convection or non-MJO phenomena over the Indo-Pacific Warm Pool is reduced.

Tracked blobs are also capable of splitting into multiple convective regions. To handle this the algorithm looks at a list of all convective blobs that meet the blob similarity threshold on frame N for a blob on frame N-1. If there are multiple bobs the algorithm chooses the largest blob to be the continuation of the blob on frame N-1 and any remaining blobs are marked as brand new events to be tracked. This only happened once for our chosen parameters for all 1640 tracked blobs across the region.

Another possible behavior is that blobs can merge together. If multiple blobs on frame N-1 match (meet our overlapping point threshold) to a singular blob on frame N the algorithm looks at the blobs on frame N-1, and whichever blob is the oldest (having been tracked for the most frames) is considered to be the main progenitor of the combined blob. The combined blob with inherit the tracking data from the oldest blob on frame N-1 and the remaining blobs will be marked as dead and tracking ceased. This merging or overlapping behavior is quite common and occurs for a large fraction of all tracked events.

As blobs are connected between frames, a record of each blob's position (determined by its geometric centroid), size, and meridional and zonal velocity between frames is produced. Combining this for all tracked events produces a database of tracked objects. This database can be refined based on any of those statistics to further limit the results to MJO events of specific characteristics. For example, focusing on events that originate in the IO and propagate through the MC we can identify events that are likely to be classical boreal winter MJO events, or by focusing on events that originate in the IO and propagate north/northeastward we can focus on BSISO events. The criteria used to refine the database to focus on boreal winter MJO events for this study are listed below. Figure 1 shows a schematic view of the tracking process for an individual MJO event.

Based on results and methodologies from previous studies such as Kerns and Chen (2016,2020) and Singh and Kinter (2020), only blobs that met the following criteria were considered to be MJO events:

1. The size must be greater than 10 pixels (62.5 deg^2).

2. Tracking must cease at least 30 degrees east of where it initiated.

3. The entire event must occur during 'boreal winter' (October 1st - May 31st) to focus predominantly eastward propagating MJO events. No events in our final sample had their tracking ceased due to this cutoff.

4. To further omit BSISO events, tracking must not end 15 or more degrees north from where it initiated and tracking is ceased north of 15N.

5. The tracking initiation longitude must be west of 115E, given our interest in MJO propagation across the MC.

6. The terminating longitude must be east of 100E

All blobs that met these criteria were considered to be MJO events. These settings were chosen to isolate the events that display the most MJO-like behavior. Events below will also be partitioned into those that propagate through versus terminate in the MC region, as described later.

2.2 Data Products:

In order to understand how surface fluxes affect MJO maintenance and propagation in the MC region for propagating and non-propagating events, a number of variables are used.

Latent heat flux (LHF), 2-meter specific humidity, sea surface temperature (SST), and 10-meter winds from Objective Analyzed air-sea FLUXes (OAFLUX) for the Global Oceans supported by NOAA's Global Ocean Monitoring and Observing (GOMO) Program and NASA's Making Earth-System data records for Use in Research Environments (MEaSUREs) Program were acquired from Woods Hole Oceanographic Institute. These data are obtained on a 1° by 1° grid, and are available from 1985-2020.

Hourly L3 Cyclone Global Navigation Satellite System (CYGNSS) Science Data Record (SDR) v3.1 surface winds (Ruf et al., 2015; Ruf et al., 2019; Gleason et al., 2021; Pascual et al., 2021) were acquired form NASA JPL's Physical Oceanography Distributed Active Archive Center (PODAAC). CYGNSS is a constellation of 8 satellites that retrieve wind speed based on characteristics of the forward scattered GPS signals from the ocean surface (Gleason et al., 2021) and represents a new way to study tropical air-sea interactions in higher detail than before. We used the "fully developed seas" version of CYGNSS. The SDR v3.1 surface winds are available starting in 2018 and run until present. To match with OAFLUX the CYGNSS SDR v3.1 winds were converted to a daily mean value and conservatively regridded to a 1° by 1° grid using the methodology of Jones (1999).

We also acquired L2 Climate Data Record (CDR) v1.0 LHFs (Crespo et al., 2019) from PODAAC which are available from 2017 to present. CDR v1.0 LHFs were converted to a 1° by 1° grid following the algorithm described in Ruf (2018). These fluxes were produced from CYGNSS wind retrievals utilizing observational and reanalysis estimates of temperature and humidity (Crespo et al., 2019). Bilinear interpolation in space was used to fill in any gaps in the data.

Daily Integrated Multi-satellitE Retrievals for GPM (IMERG) precipitation data on a 0.1° by 0.1° grid for 2000-2020 (Huffman et al., 2019) were acquired from Goddard Earth Science's Data and Information Services Center (GES DISC). IMERG combined microwave and IR precipitation estimates from satellites with other techniques such as precipitation gauge measurements to provide high-quality global precipitation estimates. To match with other datasets IMERG precipitation was conservatively regridded onto a 1° by 1° grid using the methodology of Jones (1999).

Daily 1000 hPa zonal winds from ERA5 reanalysis (Hersbach et al., 2020) were obtained from the Copernicus Climate Change Service (C3S; C3S, 2017) on a 0.25° by 0.25° for 10N-10S for 1979-2020. ERA5 reanalysis provides high spatial and temporal resolution global coverage and is the successor to ERA-Interim (ERA-I).

All data were converted to daily anomalies and then filtered using the same 30-96 day bandpass filter with a Hanning window as the NOAA Interpolated OLR data, except for 1000 hPa zonal wind data that were used to assess the background wind field during MJO events.

2.3 CESM2 Experiments:

Ahn et al. (2020) developed a propagation metric to compare simulations of the MJO for a suite of models in the 6th phase of the Coupled Model Intercomparison Project (CMIP6) against the 5th phase (CMIP5), observations, and reanalysis. This metric was defined as similarity of composite 10N-10S lag-longitude precipitation over the MC (100°E-150°E) 0.25 days after event initiation over the Indian Ocean to the calculated field for observations. Based on their metric, CMIP6 models do an appreciably better job at simulating the MJO than CMIP5 models. Further, according to the MC propagation metric of Ahn et al. (2020), the 2nd Community Earth System Model (CESM2; Danabasoglu et al., 2020) produced similar statistics to observations and reanalysis regarding the ability of the MJO to propagate across the MC. The relatively realistic MJO variability in the CESM2 makes it a suitable testbed for how MJO propagation may change under various warming scenarios.

As an Earth System Model (ESM), CESM2 models components of the Earth system including atmospheric chemistry, atmospheric circulation, radiation, plant distributions, land use, oceans, and ice to represent the Earth as a comprehensive unit with the goal of producing realistic simulations of both weather and climate. Changes to both deep-convection scheme and cloud layer parameterizatons are noted to have improved the ability of CESM2 to simulate the MJO compared to the original Community Earth System Model (Danabasoglu et al., 2020).

To investigate how MJO propagation may change in a warming climate, our tracking algorithm was applied to daily OLR output from 6 CESM2 experiments: SSP 2-4.5 (r1i1p1f1, 4.5 W m-2 forcing by 2011), SSP 5-8.5 (r1i1p1f1, 8.5 W m-2 forcing by 2011), 1% CO2 increase per year until 4xCO2 (r1i1p1f1), abrupt 4xCO2 (r1i1p1f1), and 2 historical runs (r1i1p1f1, r10i1p1f1). The MJO tracking algorithm was applied to the full length of the experiments, 86 years for SSP 2-4.5 andSSP 5-8.5, 150 years for 1% CO2, 164 years (1850-2014) for both historical runs, and 1000 years for 4xCO2. Monthly global mean near-surface temperature was acquired for the same six experiments in order to provide a measure of surface temperature change to place changes in MJO activity in context. Because our definition of boreal winter is split up by the calendar year, a year for the CESM2 experiments was redefined as being July 1st - June 30th to be boreal winter-centric.

Daily OLR data in the model simulations were filtered using the same 30-96 day bandpass filter with a Hanning window as the observational data. To focus on a wider number of MJO events, the size threshold for tracked events was lowered from 62.5 deg^2 to 11.8 deg^2, which is 10 pixels on the 1.25° x 0.94278° grid the model simulations used. Tracked MJO events within each experiment were then grouped based on 10-year global mean near-surface temperature values.

3 Observational Results

3.1 OAFLUX Results:

3.1.1 Basic Track Behavior:

Using the settings outlined in section 2.1, the tracking algorithm was applied to 34 years of 30-96 day filtered Interpolated NOAA OLR data daily anomalies, and 36 MJO events were identified. Figure 2 shows the centroid trajectories for each event as well as a heat map of where tracked events prefer to propagate. Centroid tracks in panel A were smoothed using a five-day simple moving average. For the heat map in panel B, each tracked centroid was only counted once for each pixel to prevent events that stall out over the MC from being overcounted and biasing the heat maps.

Panel B of Figure 2 shows that MJO events, when propagating into the MC region, tend to detour south of Java instead of heading eastward closer to the equator. This is expected behavior based on observations (Wu and Hsu, 2009) and is a good first order check that our algorithm is identifying typical MJO event behavior. A less common northern track is also apparent that goes directly over the islands of Sulawesi and New Guinea. These two tracks appear to reconnect near the Solomon Islands where events tend to continue propagating eastward into the equatorial Pacific. As to why both tracks converge there is unknown and outside the scope of this study. Similar density plots were produced in both Singh and Kinter (2020) as well as Kerns and Chen (2020). For Singh and Kinter (2020) these dual tracks are present and display similar behavior, yet for Kerns and Chen (2020) this behavior is missing. Events in Kerns and Chen (2020) tend to propagate directly through the MC versus detouring to the south, which may be the cause of this discrepancy. We also note that Kerns and Chen (2020) use total convective fields rather than anomalies, which may also explain some of this difference.

Figure 3 shows some statistical information for all 36 tracked events. The mean propagation speed is 2.88 m/s (Figure 3 panel D) with a mean event length of 48.8 days (Figure 3 panel C). This propagation speed is slightly slower than what observations and MJO theory suggest, 5 m/s, but is comparable to results from other tracking studies (Kerns and Chen 2016, 2020; Singh and Kinter, 2020). The convective signal from the MJO using other techniques such as lag-correlation analysis has been found to be about 4 m/s in the Indo-Pacific warm pool, which is slower than the propagation of the MJO's wind signal (e.g. Maloney and Sobel, 2004; CLIVAR MJO Working Group, 2009). The mean event length agrees with what is expected for the MJO.

The distribution for where tracking initiates (Figure 3 panel A) is approximately normal and centered around 70°E-80°E in the Indian Ocean. The distribution for where tracking terminates (Figure 3 panel B) has a bimodal appearance with a group that terminates over the MC region and another group that propagates into the Pacific Ocean. Because the two groups can be split at 150°E (roughly the eastern edge of the island of New Guinea), we refer to events where tracking ceased over the MC (100°E-150°E) as terminating events, and events that propagated out into the Pacific Ocean as persisting events. We end up with 18 persisting events and 18 terminating events using this definition, a similar ratio to that of Kerns and Chen (2016, 2020). This natural distinction between the two groups lines up with the known impact of the MC's 'barrier effect', where the MJO weakens and potentially dissipates before reaching the Pacific Ocean (Ling et al., 2019; Salby and Hendon, 1994; Zhang and Ling, 2017).

As a first order approach to understand why some events propagate through the MC region, we compare the tracking for both classes of events in Figure 4. As in Figure 2 the tracks in panels A and B were smoothed using a five-day simple moving average. The track density panels (Figure 4 panels C and D) show that a large difference does not exist between the two categories in terms of where they prefer to initially propagate. Both groups start to detour south of Java, although terminating events do tend to go slight further south towards the northwestern coast of Australia. The 'barrier effect' of the MC does not appear to be generally dependent on the path by which the MJO convective disturbance originally enters the MC.

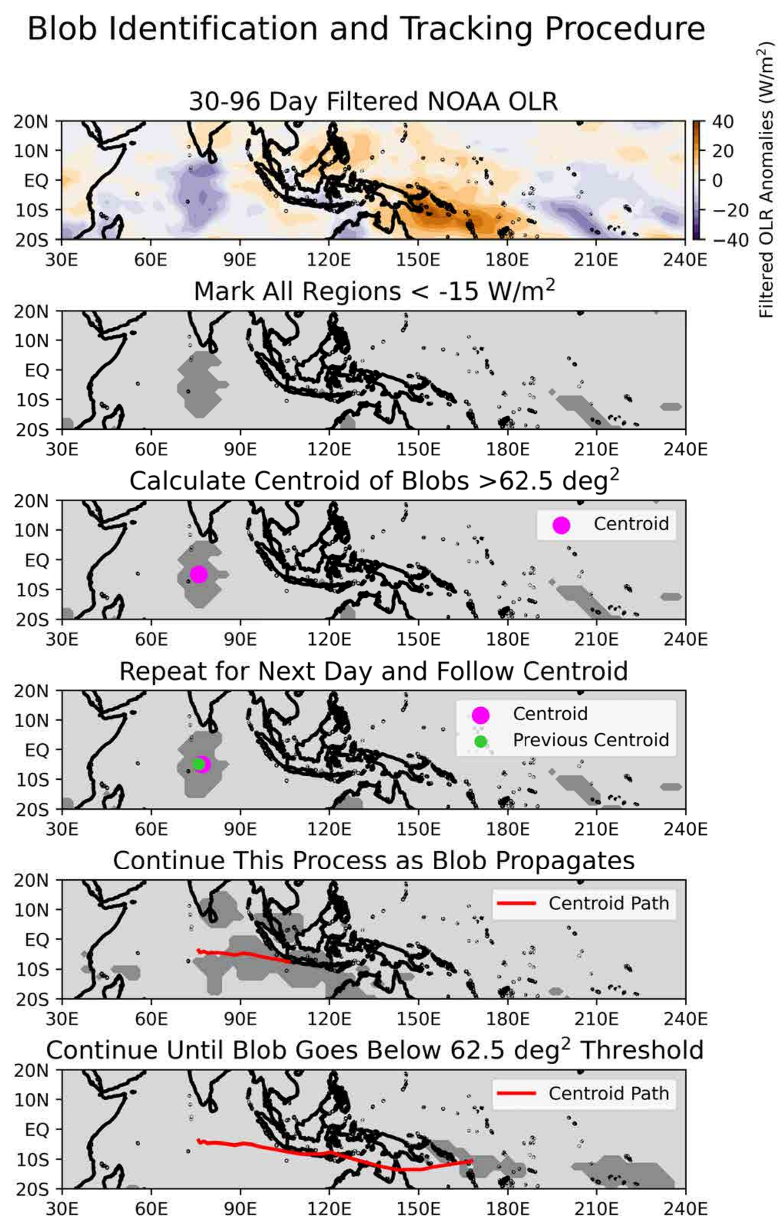

Figure 1: A schematic view of how our tracking algorithm works. We take intraseasonally filtered NOAA interpolated OLR data and produce binary maps to highlight regions with anomalies less than -15 W/m^2. Our algorithm then identifies regions greater than a specified size threshold and follows them as they propagate through time, storing the position of the geometric centroid on each day. Using this we can reconstruct the path taken by an MJO event as it propagates.

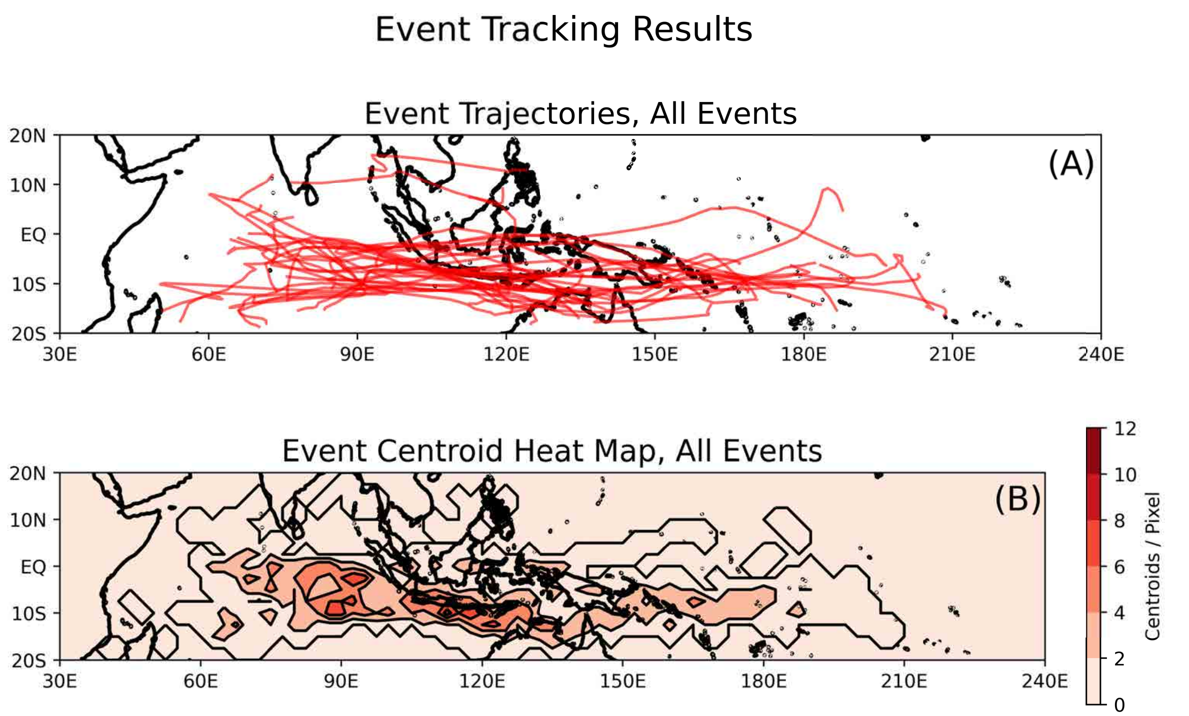

Figure 2: MJO event tracking results from applying our algorithm to NOAA Interpolated OLR data. In panel A we see individual MJO event tracks and in panel B we see a heat map of where MJO events prefer to propagate. As expected MJO events prefer to detour south of the MC region following along the southern coast of Java.

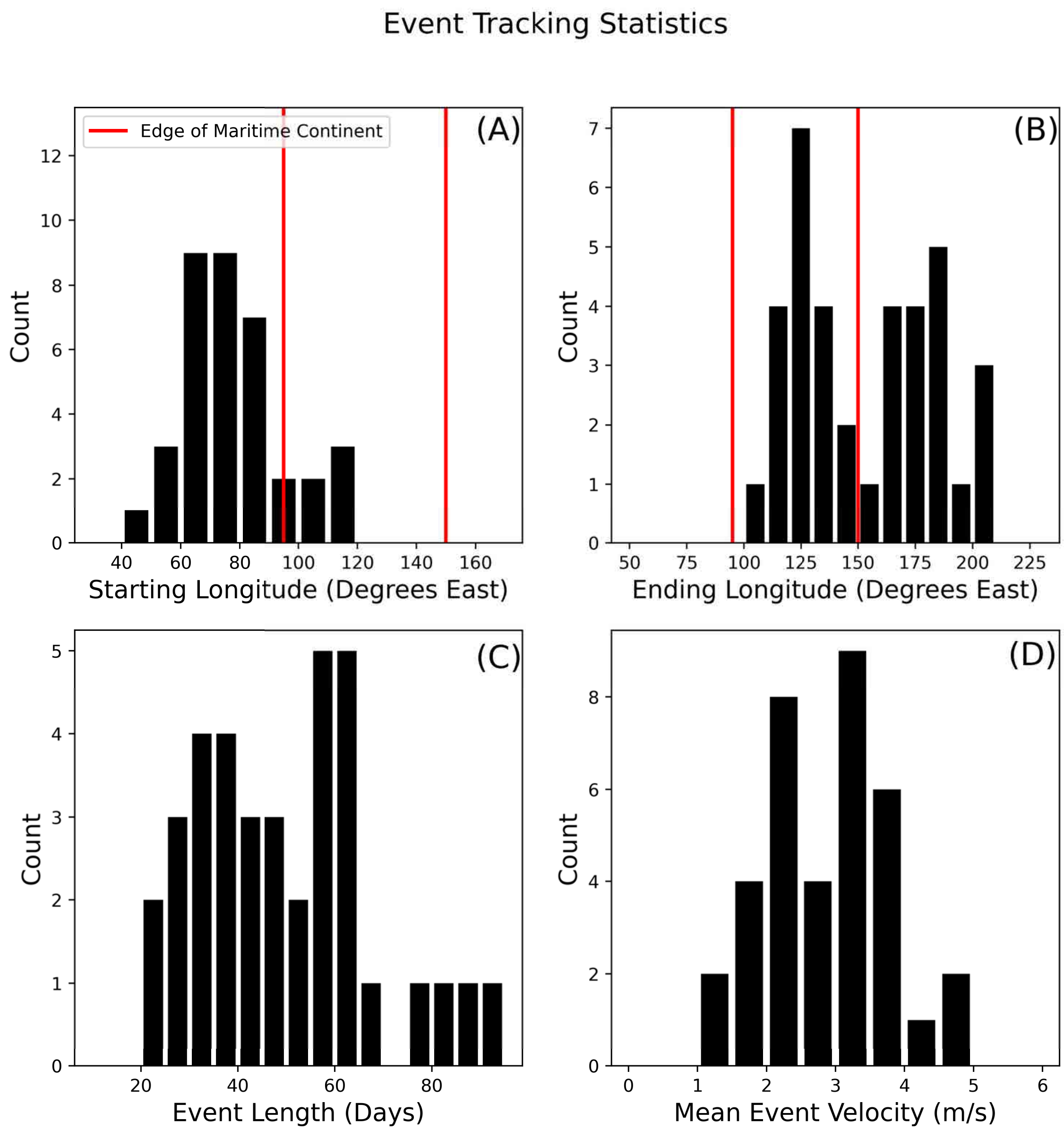

Figure 3: Distributions of where our algorithm began tracking MJO events (Panel A), ceased tracking MJO events (Panel B), how long each MJO event was tracked (Panel C), and the mean propagation speed of each MJO event (Panel D). A clear bimodal distribution can be seen in panel B which we use to divide MJO events into persisting and terminating categories.

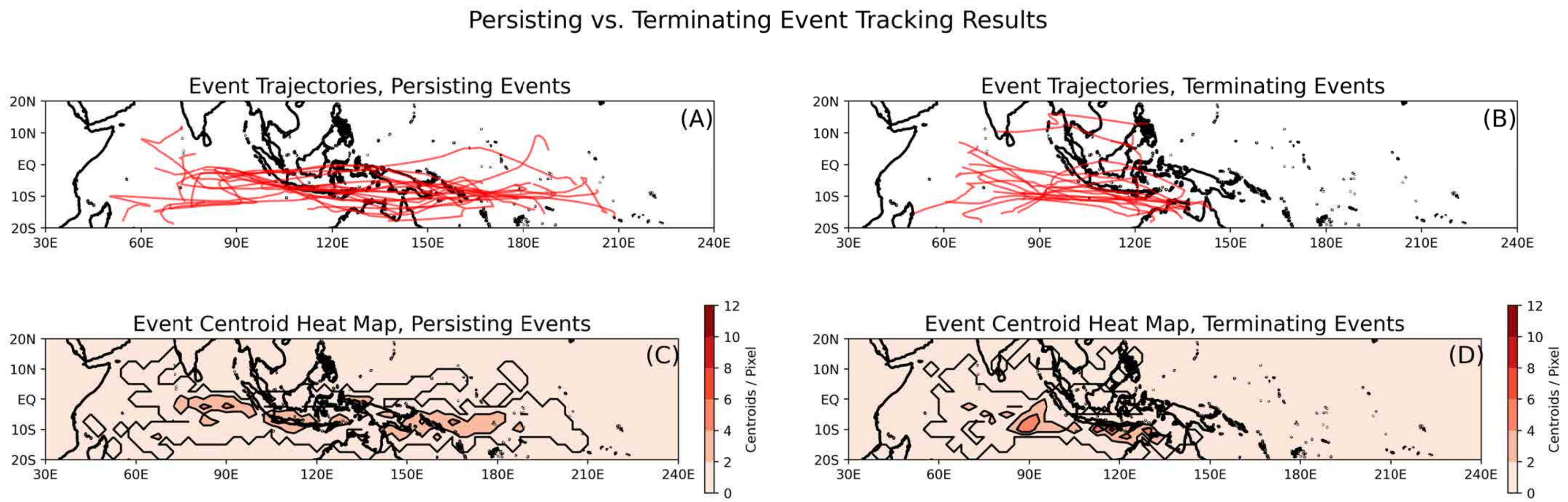

Figure 4: Similar to Figure 2 except the persisting and terminating event categories have been separated. We can see that both classes of events have similar preferred propagation paths which suggest that whatever sets them apart is not a matter of where they propagate.

3.1.2 Surface Fluxes and Local Feedbacks onto Terminating versus Propagating Events

Examination of local surface variables is conducted to provide physical insight into propagating versus non-propagating events, viewed through the lens of moisture mode theory. The ratio of OLR and LHF anomalies to precipitation anomalies (measured in W/m^2) has been used in the context of moisture mode theory to better understand what role radiative feedbacks and surface flux feedbacks play in MJO maintenance and propagation (e.g. Adames and Kim, 2016; Bui et al., 2020; Riley Dellaripa and Maloney, 2015). To understand the evolution of these ratios along the MJO tracks, a 10 degree latitude by 30 degree longitude box centered on a tracked convective region's geometric centroid was considered for every day of tracking. The spatial mean of OLR, LHF, and precipitation anomalies in this box were calculated for every day of tracking and related to the center of the corresponding grid cell's longitude (e.g. A centroid located at 64.4°E would be placed into the 65°E grid cell's results). The absolute ratio of OLR and LHF anomalies to precipitation anomalies (converted to W/m^2 using latent heat of vaporization) was then calculated and composited for both persisting and terminating events and plotted in Figure 5. Because the precipitation dataset we use is more limited in time than that for LHF and OLR, we limited this analysis to only the events that occurred from 2001-2019. Due to high sensitivity to a small number of days the first three longitude bins for terminating events were removed from this analysis, our results are not qualitatively sensitive to these data points.

Over the course of all event tracking the mean absolute ratio of LHF to precipitation is 0.073 for persisting events and 0.083 for terminating events. Over the Indian Ocean (IO) these values are slightly lower, 0.042 for persisting events and 0.046 for terminating events. In the MC region this trend is reversed and values are slightly higher 0.117 for persisting events and 0.109 for terminating events. For persisting and terminating events the value of this ratio evolves pretty similar over regions where both are tracked, both start out low over the IO (except for the first longitude band for terminating events) before rising over the MC region hitting maxima around 125-140E which coincides with where tracking is most likely to be ceased for terminating events. The ranges for these ratios also agree well with the range of values calculated by Bui et al. (2020) and Riley Dellaripa and Maloney (2015) of 4-12%. In general, it does not appear that the ratio of LHF to precipitation anomalies is substantially different for terminating versus propagating events, suggesting that changes in the strength of surface flux feedbacks are unlikely to explain the differences between these types of events.

The absolute ratio of OLR to precipitation evolves similarly, with mean values of 0.185 and 0.205 for persisting and terminating events respectively. Like with LHF, these values increase from the IO where mean values of 0.190 for persisting events and 0.202 for terminating events are found, to the MC where mean

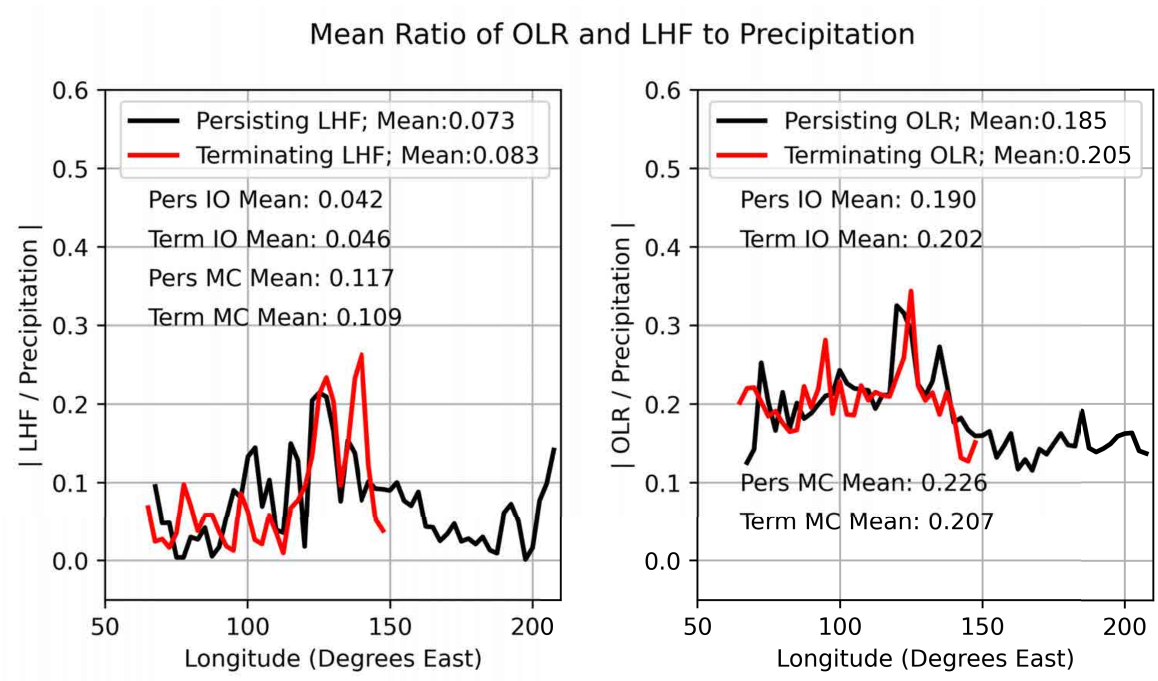

Figure 5: Absolute ratio of LHF and OLR to precipitation in a 30 degree longitude, 15 degree latitude box around tracked event geometric centroids for every day of tracking for both persisting and terminating events. Across the entire tracking period the mean ratio is similar for across both values for both categories.

values of 0.226 for persisting events and 0.207 for terminating events occur. Values over the MC have notable rise around 125E. Overall, a range of mean values of 0.185-0.226 for the ratio of negative OLR anomalies to precipitation anomalies occurs in these areas, which is slightly higher but still generally in agreement with the values over similar regions of 0.16 over the IO from Bui et al. (2020), and 0.17-0.2 from Adames and Kim (2016). Only subtle differences in these ratios occur for persisting versus terminating events using this method.

Next, Maps of LHF, SST, and precipitation anomalies were composited relative to the convective centroid using the following technique. For every day an event was tracked, a 30 degree latitude and 100 degree longitude box centered on the convective feature's geometric centroid was considered, similar to the process to produce Figure 5. OLR, LHF, SST, and precipitation anomalies values within this box were then averaged across every day of tracking to produce composite spatial distributions of the MJO related variables in latitude and longitude coordinates relative to the centroid. Fields were bandpass filtered to 30-90 days before compositing.

Figure 6 shows a centroid centric composite for OAFLUX LHF (colors) and OLR (contours) over the entire tracking period for all events, as well as composites separated into persisting and terminating events. For persisting events relative to terminating events, the spatial distribution of both OLR and LHF covers a much larger spatial area. We note that Wang et al. (2019) showed that climate models with convective events confined to relatively small spatial areas have difficulty propagating the MJO across the Maritime Continent. The distribution of LHF for persisting events shows a higher spatial coherence with a clear core region that is zonally oriented. The LHF distribution for terminating events has no clear core and is oriented in a NW-SE fashion. Despite these differences in LHF coherence, both categories have similar ratios of LHF to precipitation anomalies across the entire length of the tracks (Figure 5).

To understand why terminating events end their tracks in the Maritime Continent region, we partitioned composites into individual regions. Hence, similar centroid centric composites were produced but only for segments of tracks over the Indian Ocean (30-100E; Figure 7) and over the MC region (100-150E; Figure 8). In Figure 7 it can be seen that over the Indian Ocean, persisting events have substantially stronger and more coherent LHF anomalies in regions of convection despite having a similar ratio of both LHF and OLR anomalies to precipitation (Figure 5). This stronger support by LHF for propagating events would tend to maintain MJO convective anomalies as described in moisture mode theory (e.g. Sobel and Maloney 2013). Strong westerly wind bursts would also tend to advect these enhanced LHFs into the core of the precipitation region helping to support persisting events. As events progress into the MC region (Figure 8), the composite LHF gets stronger on average for both persisting and terminating events, but persisting events tend to have stronger and more spatially coherent LHF anomalies relative to terminating events despite the ratio of area-averaged LHF to precipitation for terminating events rising to a max value of 0.26.

Over the lifetime of tracked events LHF appears to provide more energy in regions of MJO convection anomalies, and over a larger area that is comparable in size to the core region of convection for persisting events. Local LHF enhancement and coherence with convection may play an important role in helping to provide energy and moisture to the MJO that helps events overcome the ‘barrier effect’ of the MC. Making the assumption that convection is locally supported by moisture as in moisture mode theory (e.g. Adames and Kim 2016), these fluxes may thus help to augment other processes that have been cited as important for propagating the MJO through the Maritime Continent, including the effects of horizontal moisture advection (e.g. Kim et al. 2014; Ahn et al. 2020). Because terminating events appear to on average generate less LHF locally despite having a similar ratio of LHF to precipitation as persisting events, the reduced moisture and energy may help to limit the ability of the MJO to propagate through the MC.

Similar centroid centric composite maps were generated to analyze precipitation (Figures 9, 10, 11) and SST (Figures 12, 13, 14). Because IMERG precipitation begins in the middle part of the year 2000, we only included the MJO events that occurred between 2001 and 2019 for the precipitation composites. When viewed for composites over the course of the entire event, terminating events appear to produce much less precipitation and have a smaller spatial scale than for persisting events (Figure 9). For persisting events the region that receives at least 2 mm/day of precipitation is roughly double the area of the equivalent region for terminating events. This narrower zonal structure for MJO events that terminate is consistent with that found in Wang and Lee (2017), where broader zonal convective structures foster strong Kelvin wave dynamical responses to the east of MJO convection that foster propagation. Over the Indian Ocean region (Figure 10), a similar size discrepancy is observed. In addition, precipitation for terminating events appears to be more spatially coherent than persisting events. As events propagate into the MC region (Figure 11) the precipitating region for persisting events becomes substantially larger than the equivalent region for terminating events, and precipitation anomaly magnitudes are generally larger, although high localized composite rainrates can still occur for terminating events.

To first order, SST anomalies associated with MJO events are produced by latent heat and shortwave radiation fluxes during MJO events, although ocean dynamics can modulate the strength of this signal (DeMott et al. 2015). Figure 12 shows that over the entire event track, persisting events have a more pronounced cooling effect on the ocean, a signal consistent with the enhanced LHF of persisting events. Isolating events as they propagate through the Indian Ocean region (Figure 13), differences are even more readily apparent. Terminating events have less than half the impact on SST that persisting events do, and are preceded by SST anomalies to the east that are not quite as warm. These weaker SST anomalies to the east would not only suppress the thermodynamic component of surface fluxes to the east of MJO convection (DeMott et al. 2015; see eq. 1 below), but would also suppress other mechanisms that help propagate the MJO eastward, such as frictional moisture convergence (deSzoeke and Maloney 2019), and moistening by shallow convection (e.g. Ruppert and Johnson 2015). In Figure 14 composite SST anomalies increase to the southeast of of convection for terminating events, but this is not enough to overcome the weakening of convection and LHF that is occurring over this region.

The first part of this analysis took a local view of the ability of surface fluxes to support MJO convection through the Maritime Continent region, through the lens of moisture mode theory. Looking at local impacts of LHF and SST on MJO propagation, over the Indian Ocean and in the Maritime Continent, terminating events appear to have a decreased ability to extract moisture from the ocean despite similar local ratios of OLR and LHF anomalies to precipitation anomalies as persisting events. Further, as events propagate through the MC region, terminating events become more spatially concentrated compared to persisting events, which may limit their ability to propagate eastward.

3.1.3 Global View of MJO Fluxes During Propagating and Terminating Events:

Studies such as Raymond and Fuchs (2018) argue that the MJO should be viewed as a global mode in which the MJO exists within a regime of low level zonal easterly flow. Easterly MJO anomalies add constructively to this easterly mean flow to produce an wind-driven enhancement of surface fluxes to the east of MJO convection that causes eastward propagation. This view argues that the local processes underpinning the MJO in the Maritime Continent do not exist in a vacuum, and the conditions of the tropics at large can have an impact on MJO propagation through the MC. Hence, this section examines the larger scale factors that potentially play into MJO propagation through the Maritime Continent.

Because we are directly tracking individual events, we can exactly define when events propagate through particular regions of the tropics. Instead of using the traditional 8 phases that other studies have used to define MJO evolution (e.g. Wheeler and Hendon 2004), we can instead make time lagged global composite relative to when the MJO centroid crosses a certain location. Because we are particularly interested in understanding how the 'barrier effect' of the MC impacts the MJO, we can look at global behavior relative to the time when MJO events propagate into the MC region.

Figure 15 shows time-lagged global composites of LHF between 30N-30S and 30-300E, relative to when MJO events propagate across 100E into the MC region. For the 5 events that tracking initiated east of 100E the day tracking initiates was used as the day on which 100E was crossed. Removing these events did not qualitatively change our results. Looking at the time 5 days before events cross 100°E, persisting events show substantially elevated LHF across the central and eastern equatorial Pacific and reduced LHF over the MC compared to terminating events. At day 0, persisting events continue to show enhanced LHF across the central and eastern equatorial Pacific as LHF anomalies are modest in that region for terminating events. At day +5, enhanced LHF associated with persisting events is elevated near the southern coast of Java, whereas enhanced flux anomalies with terminating events are found further south near the NW coast of Australia. At this time, the equatorial region of enhanced LHF over the Central Pacific Ocean for persisting events begins to transition toward negative LHF anomalies as the MJO convective center propagates into that region (e.g. see Figure 16).

The large region of enhanced LHF anomalies that occurs near and to the east of the Dateline for propagating events is a notable signal compared to terminating events., although it is possible that this flux signal could be the remnants of a preceding MJO event that our method did not pick up. To investigate this and further support the potential importance of this Central and Eastern Pacific flux anomaly for supporting MJO propagation through the Maritime Continent, Hovmöller diagrams of LHF from 10°N-10°S were generated for composites relative to 100°E crossing events (Figure 16). For persisting events, a strong

LHF anomaly is present over the central and eastern equatorial Pacific as the MJO begins to transition into the Maritime Continent, whereas for terminating events it is absent. This LHF feature is relatively stationary, appearing over the equatorial pacific roughly 15 days before persisting events enter the MC region, and lasting for roughly 25 days. At first glance, the appearance of this LHF anomaly for persisting events is consistent with arguments made in Sentić et al. (2020) and related studies that MJO propagation and dynamics are supported by large-scale enhanced surface fluxes to the east of MJO convection in the presence of mean equatorial easterly flow.

A major question is the extent to which this large-scale flux signal for persisting events is primarily wind-driven, versus having a strong thermodynamic component. Figure 17 is a composite of SST anomalies relative to the time when MJO events propagate into the MC region, similar to Figure 15. Persisting events have positive SST anomalies on the order of 0.05-0.2K over the Central and Eastern Pacific, larger than the SST anomalies of order 0.05-0.15K in the same region for terminating events, which also appear to be more geographically isolated. It is possible the larger SST anomalies near and to the east of the Dateline for persisting events may contribute to the flux anomaly signal we see in the composites (e.g. Figures 15 and 16).

To further investigate potential causes behind this LHF anomaly, we deconstruct LHF anomalies into dynamic and thermodynamic components in three regions of the tropics (Eq. 1). The first region is over the Indian Ocean (IO Box; 0-10°S, 80°E-100°E), the second region is over the MC where most events propagate through (MC Box; 5°S-15°S, 120°E-140°E), and the final region is situated over the core of the observed LHF anomaly in the Central and East Pacific (PA Box; 10°N-10°S, 180°E-200°E). The flux decomposition is conducted as follows:

$$LH' = \rho L C_H (\overline{\Delta q}|V|' + \Delta q' \overline{|V|}) \tag{1}$$

Here, LH' represents intraseasonal LHF anomalies, represents density, L is the latent heat of vaporization of water, and CH is an exchange coefficient. The LCH term is represented as an arbitrary scaling factor that is kept constant at a value of 3000 and produces a good fit to the total flux anomaly derived from OAFLUX (e.g. see also Maloney and Esbensen 2005). q is the difference in specific humidity between the surface of the ocean and 2 meters above it, where 2 meter specific humidity from OAFLUX was used. To calculate ocean surface specific humidity we assumed that the air at the ocean surface was of a similar temperature to the ocean surface and is fully saturated. With these assumptions, OAFLUX SSTs were used to calculate surface specific humidity. $|V|$ represents the magnitude of OAFLUX 10m winds (the lowest available level). Primes represent intraseasonally filtered anomalies and overbars represent unfiltered composite means for the duration of each tracked MJO event. A similar decomposition was conducted in Maloney and Esbensen (2005) to examine the influence of thermodynamic versus wind-driven variability in producing east Pacific intraseasonal flux variability during boreal summer.

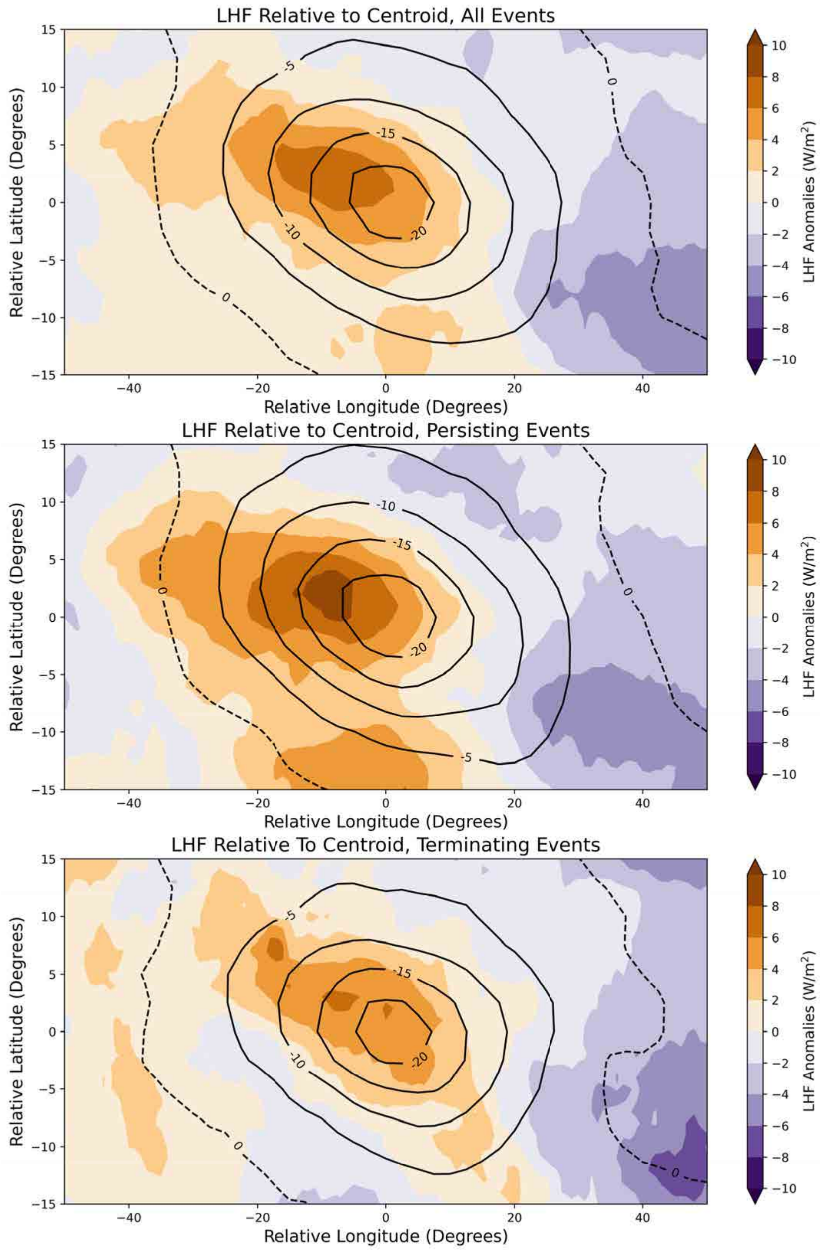

Figure 6: Composite centroid centric plots of LHF (color) across the entire track for all events (top panel), persisting events (middle panel), and terminating events (bottom panel). Contours are composite OLR anomalies in W/m2. We can see that for persisting events LHF is stronger and more spatially coherent compared to terminating events which also have a NW-SE directionality.

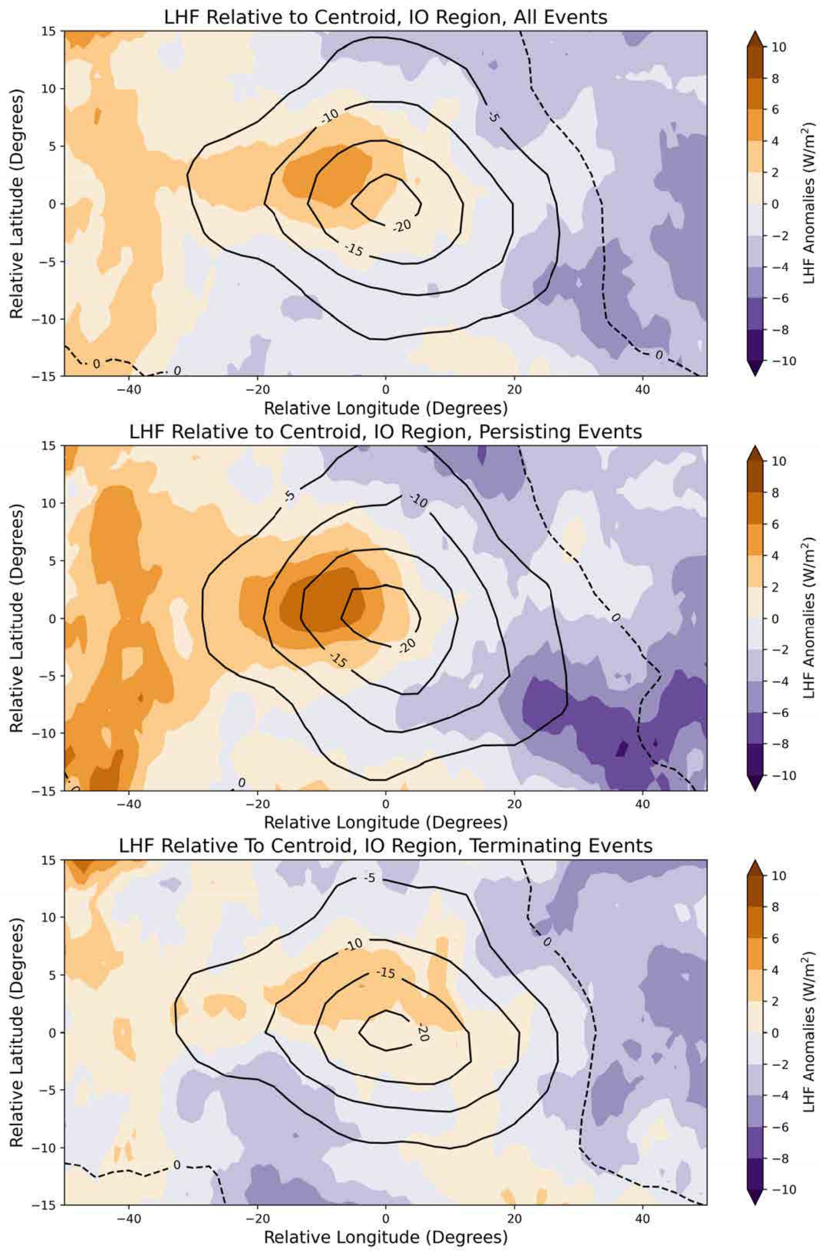

Figure 7: Similar to Figure 6 except for just over the Indian Ocean 30 – 100E. The LHF for persisting events is much stronger compared to that of terminating events.

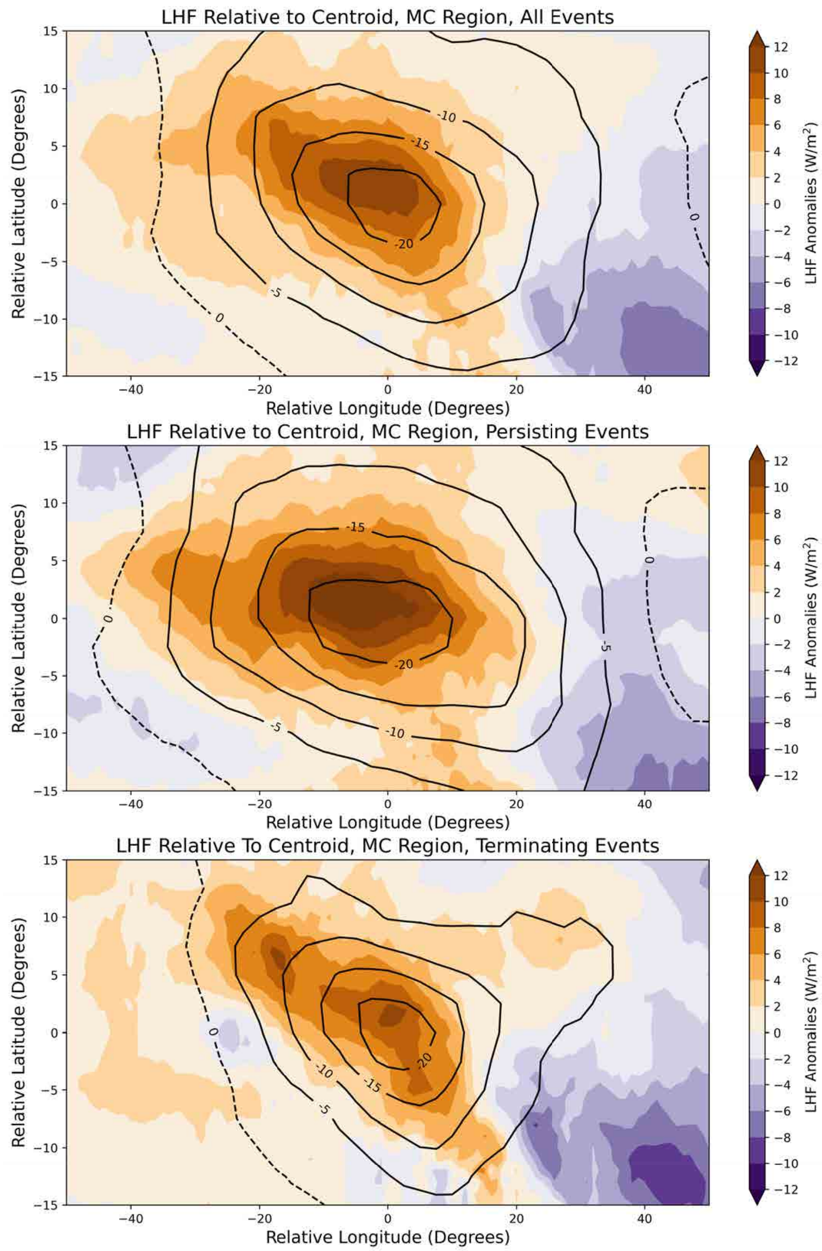

Figure 8: Similar to figure 6 except for just over the MC region 100 - 150E. LHF and OLR cover a much wider region for persisting events and are zonally oriented versus the NW-SE tilt of terminating events.

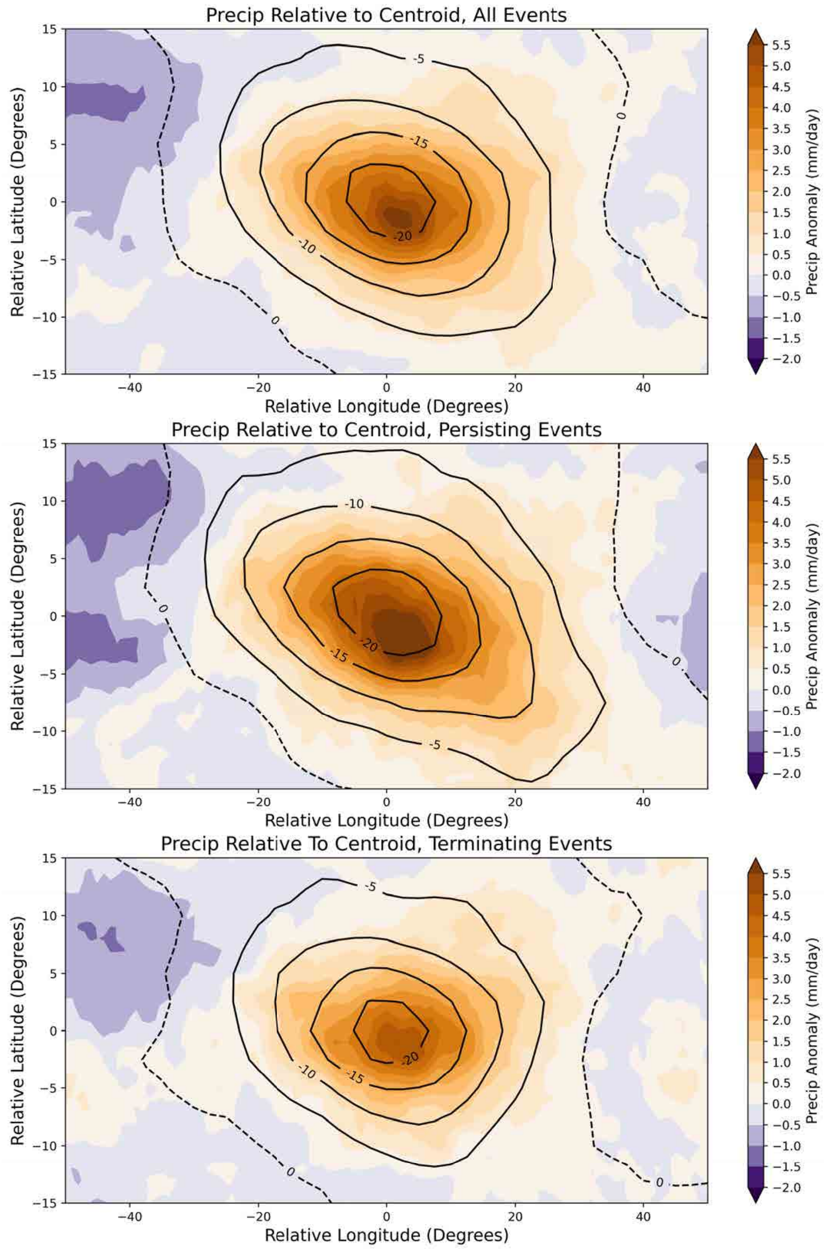

Figure 9: Similar to figure 6 except for precipitation anomalies (color). Limited to only events from 2001-2019 due to the length of IMERG precipitation data. We see that over the entire course of an events lifetime persisting events on average have a much larger convective region with higher mean precip.

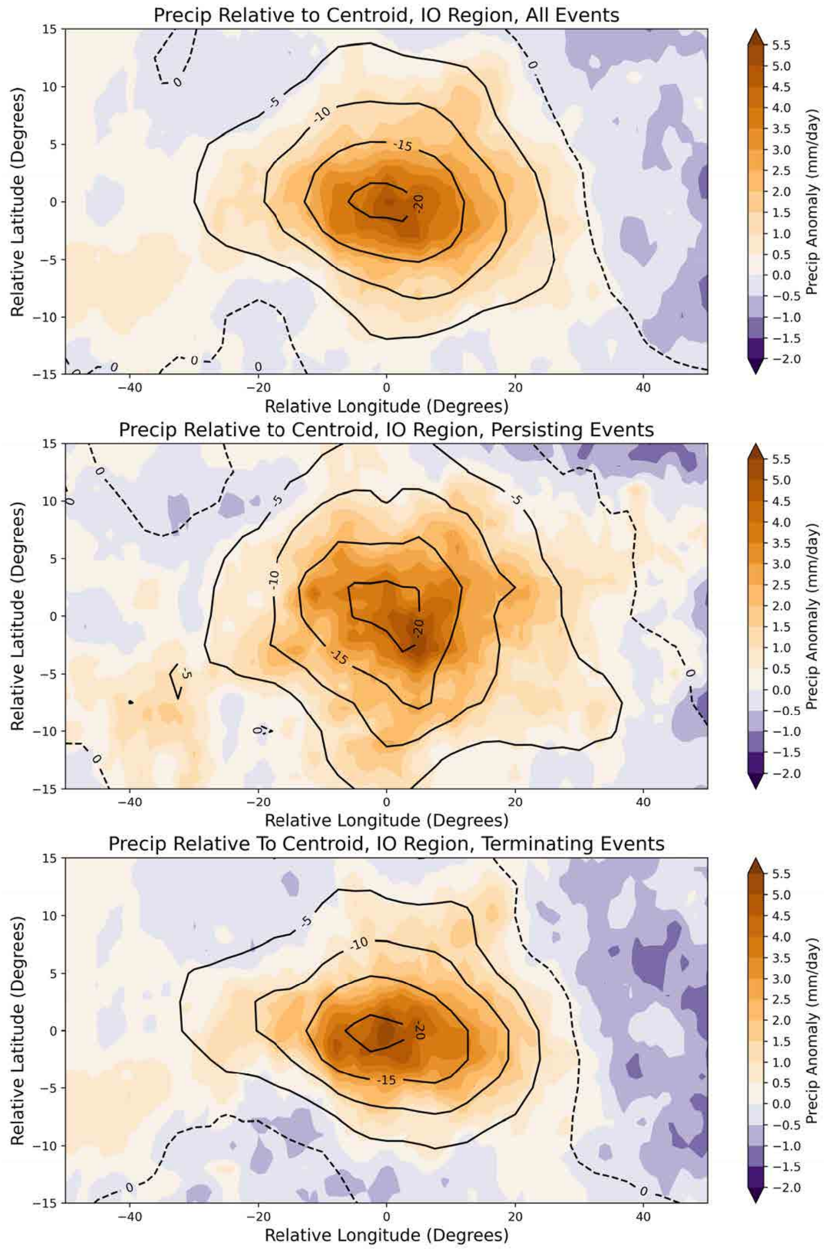

Figure 10: Similar to figure 7 except for precipitation anomalies (color). Limited to only events from 2001-2019 due to the length of IMERG precipitation data. Over the Indian Ocean terminating events have much more coherent precipitation with similar precipitation rates to persisting events.

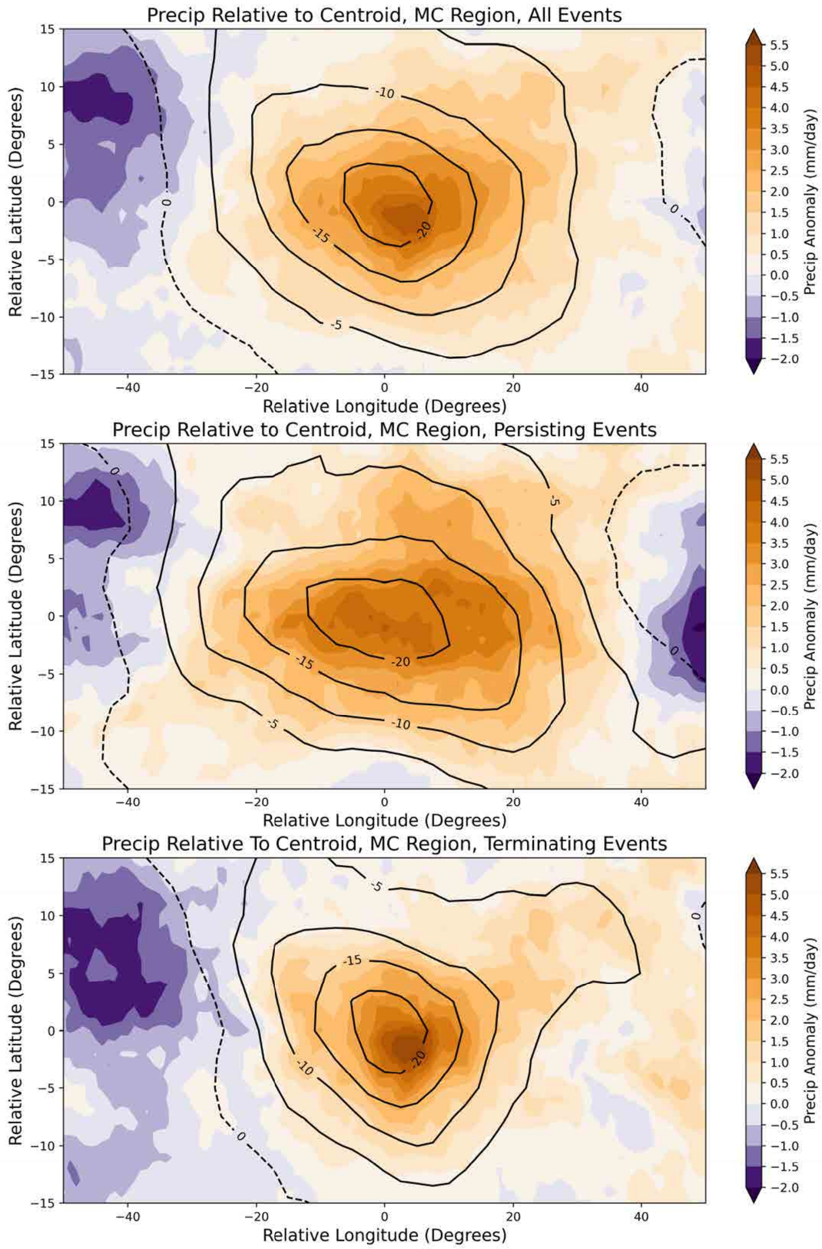

Figure 11: Similar to figure 8 except for precipitation anomalies (color). Limited to only events from 2001-2019 due to the length of IMERG precipitation data. Over the MC region terminating events have higher peak precipitation anomalies over a significantly smaller area compared to precipitation events.

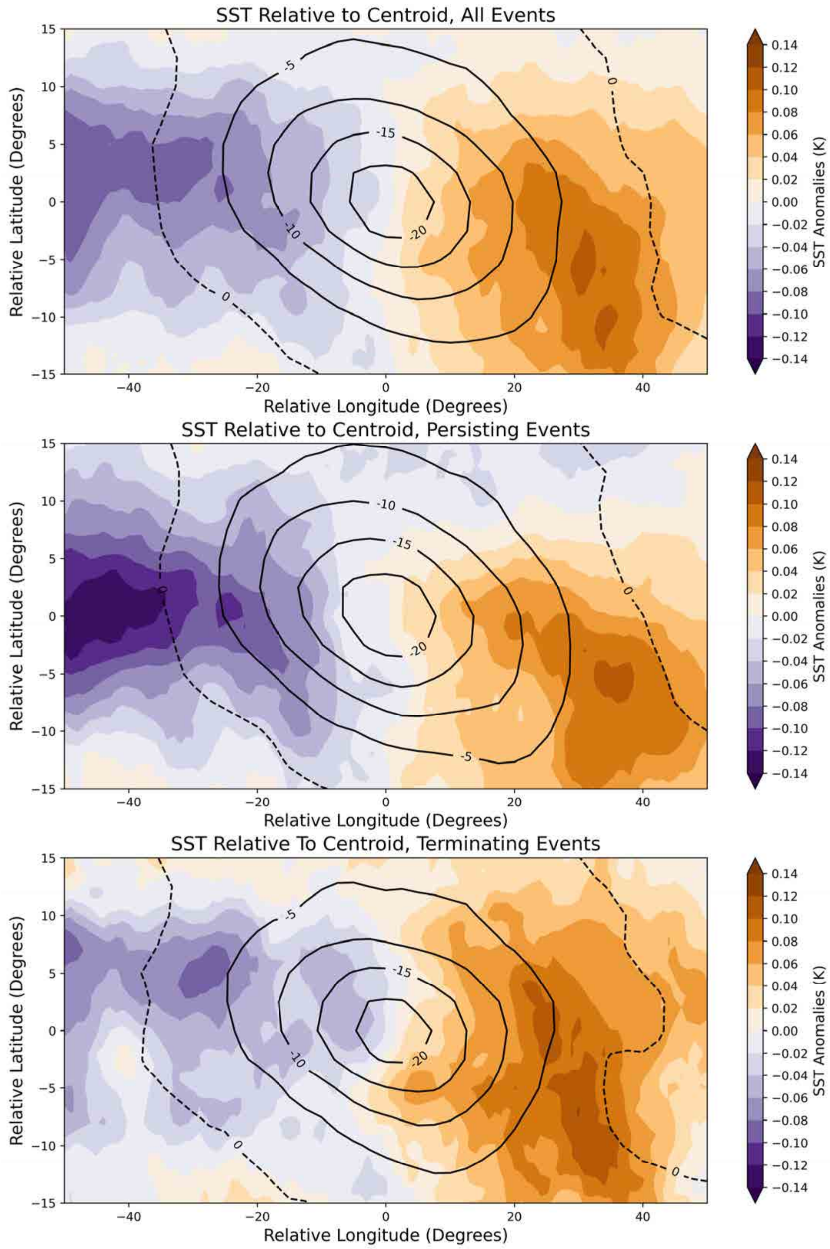

Figure 12: Similar to figure 6 except for SST anomalies (color). Persisting events appear to have a much stronger impact on SST compared to terminating events which agrees with the enhanced LHF we observe in figure 5.

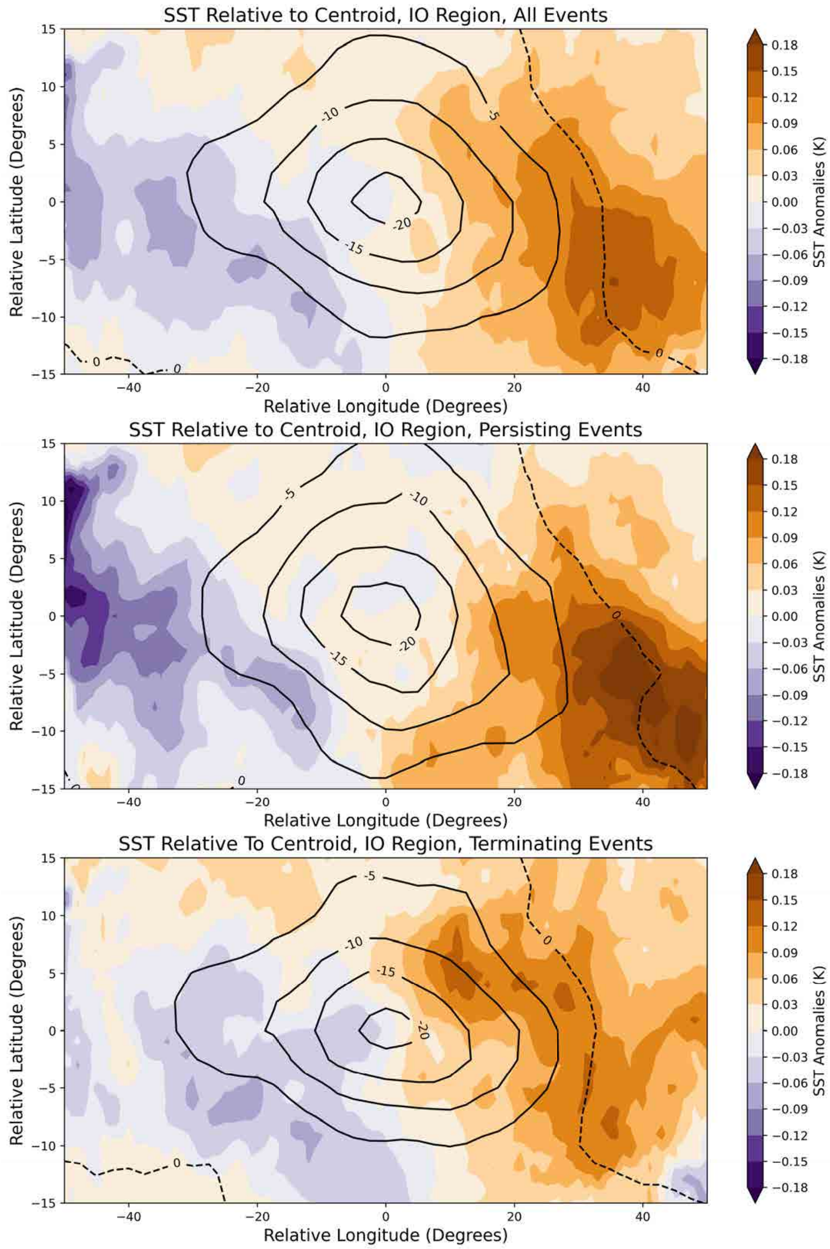

Figure 13: Similar to figure 7 except for SST anomalies (color). Over the Indian Ocean persisting events tend to propagate into much warmer waters and manage to cool the ocean behind them by approximately 0.3K.

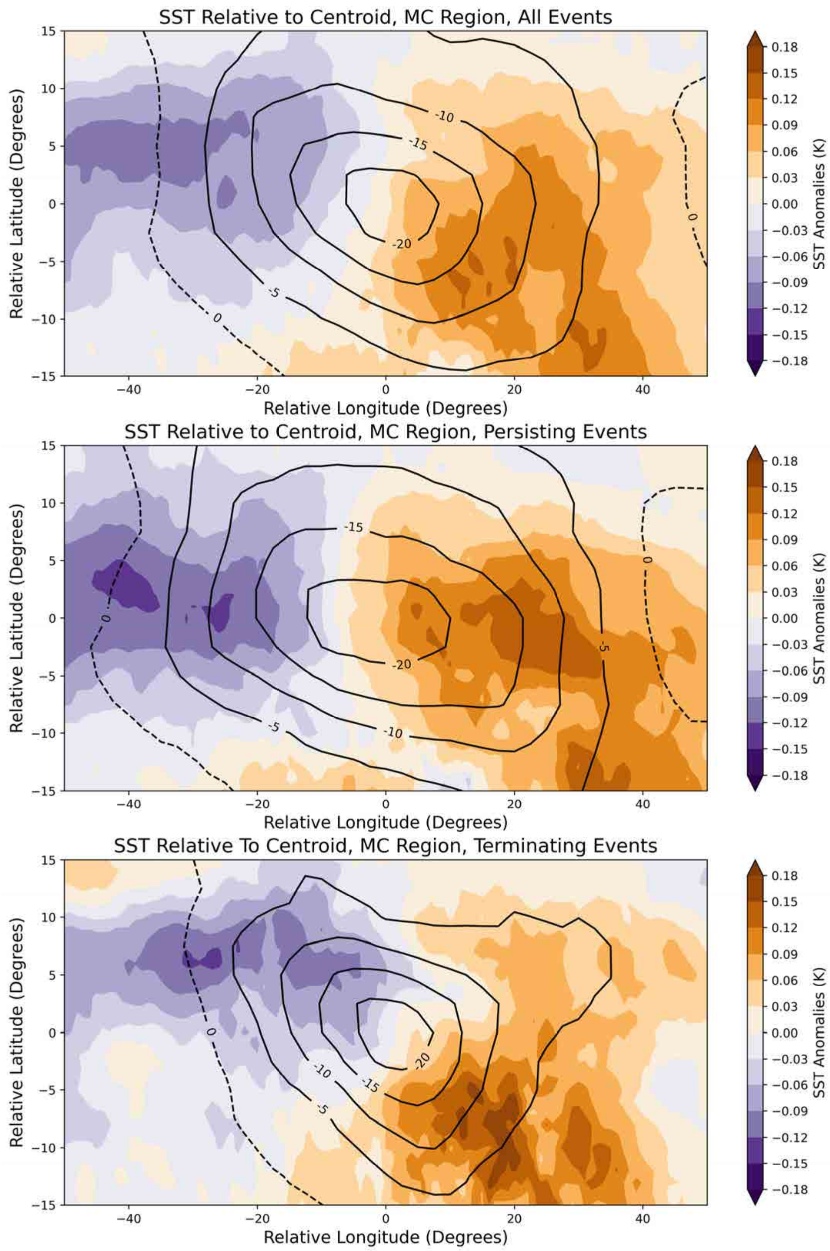

Figure 14: Similar to Figure 8 except for SST anomalies (color). We see that the SST anomalies for terminating events display the same NW-SE alignment as OLR and LHF.

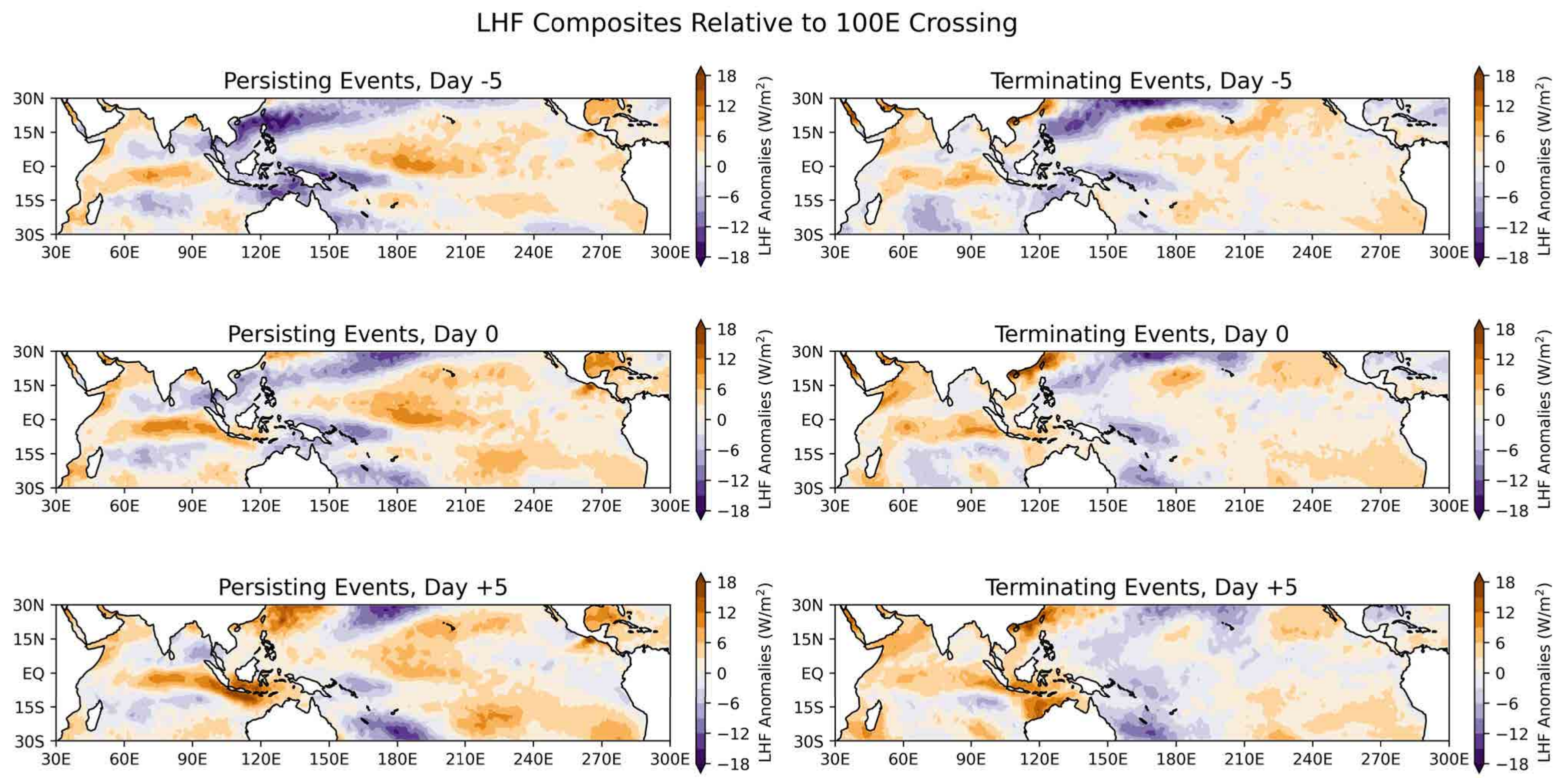

Figure 15: LHF composites of persisting events -5, 0, and +5 days relative to the tracked centroid crossing 100°E. We see that persisting events have a stronger negative LHF anomaly over the MC region as well as a large positive LHF anomaly that covers most of the equatorial pacific which is absent in terminating events.

Figure 18 shows a map of the three boxed regions as well as the LHF decompositions of Eq. 1. for all events, persisting events, and terminating events. For the IO Box and the MC Box, wind anomalies dominate driving of the LHF anomaly, which agrees well with previous results for the MJO in these regions (DeMott et al., 2014; Riley Dellaripa and Maloney 2015). In the PA Box, for persisting events the LHF anomaly is of a similar magnitude as for the IO Box, although the LHF anomaly is driven approximately equally by a mixture of thermodynamic and dynamic components. This differs from the WISHE model of Raymond and Fuchs (2018), where the flux anomaly to the east of MJO convection was primarily wind-driven. For terminating events, the LHF anomaly in the PA box is greatly reduced and is driven almost entirely by thermodynamic effects. DeMott et al. (2014) used three different versions of the Community Atmosphere Model (CAM) to investigate ocean coupling in simulations of intraseasonal oscillations (e.g. the MJO). They found that the fraction of MJO-related LHF over the Dateline and east Pacific region associated with the thermodynamic component (q) was less than 20%. This represents a discrepancy with our results which place this fraction at 50%.

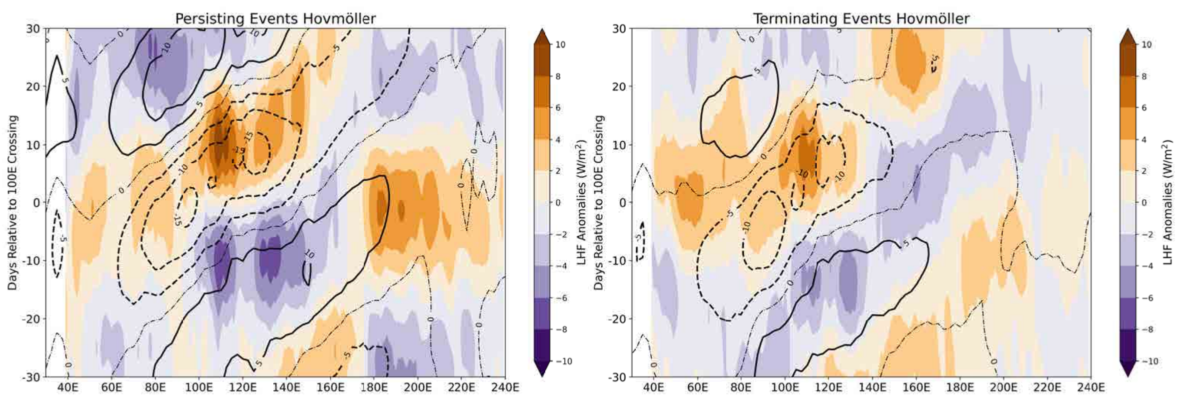

Figure 16: Composite Hovmöller diagrams of LHF (color) and OLR (contours) for -30 to +30 days relative to the tracked centroid crossing 100E. Meridional mean is from 10°N-10°S. We see that the positive LHF anomaly between 180-240E is present for persisting events but absent for terminating events. The positive LHF anomaly also appears to be stationary in time meaning it is not an MJO produced phenomena.

We briefly return to the paradigm of the MJO as a moisture mode, and examine the strength of flux anomalies relative to precipitation in the boxes defined in Figure 18, to assess how important fluxes are relative to radiative feedbacks in helping to maintain the MJO in these regions (e.g. Bui et al. 2020). When precipitation is expressed in W/m^2, fluxes anomalies have been found to be approximately 4-12% of the magnitude of precipitation in the Indian Ocean and west Pacific (Bui et al., 2020; Riley Dellaripa and Maloney, 2015). Using the same boxes as our LHF decomposition, we examined the relationship between LHF, precipitation, and OLR (Figure 19). To compare the results of our tracking against those of the OMI index we plotted the relationships between these variables for days where the OMI index was greater than

1 (red points in Figure 19), indicating possible MJO behavior, and days that our algorithm was actively tracking one of our 36 events (black points in Figure 19).

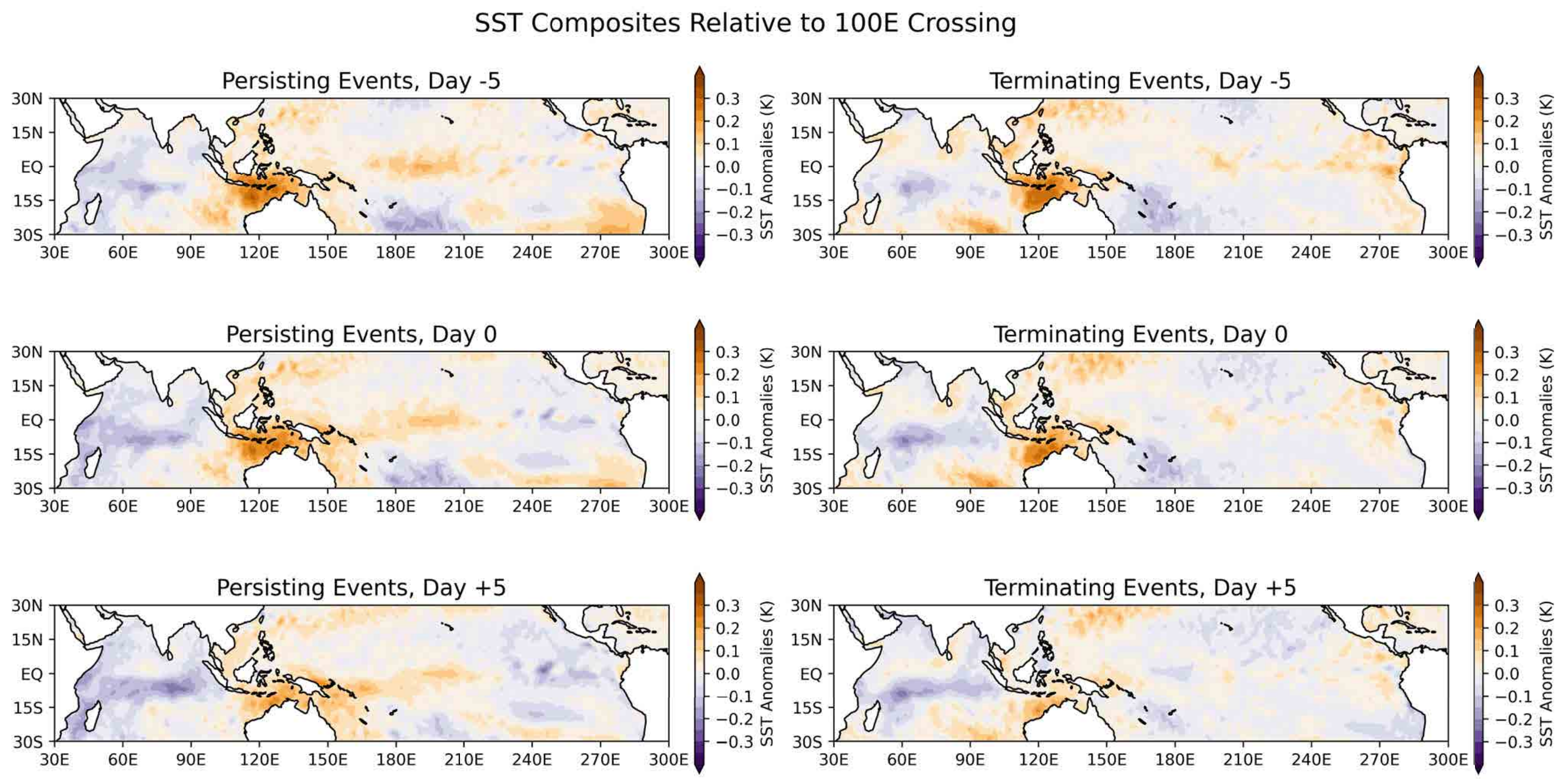

Figure 17: Figure 17: Same as figure 15 but for SST anomalies. We see that persisting events have elevated SST anomalies over the equatorial pacific relative to terminating events hinting that the LHF anomaly in that region may not be entirely wind-driven.

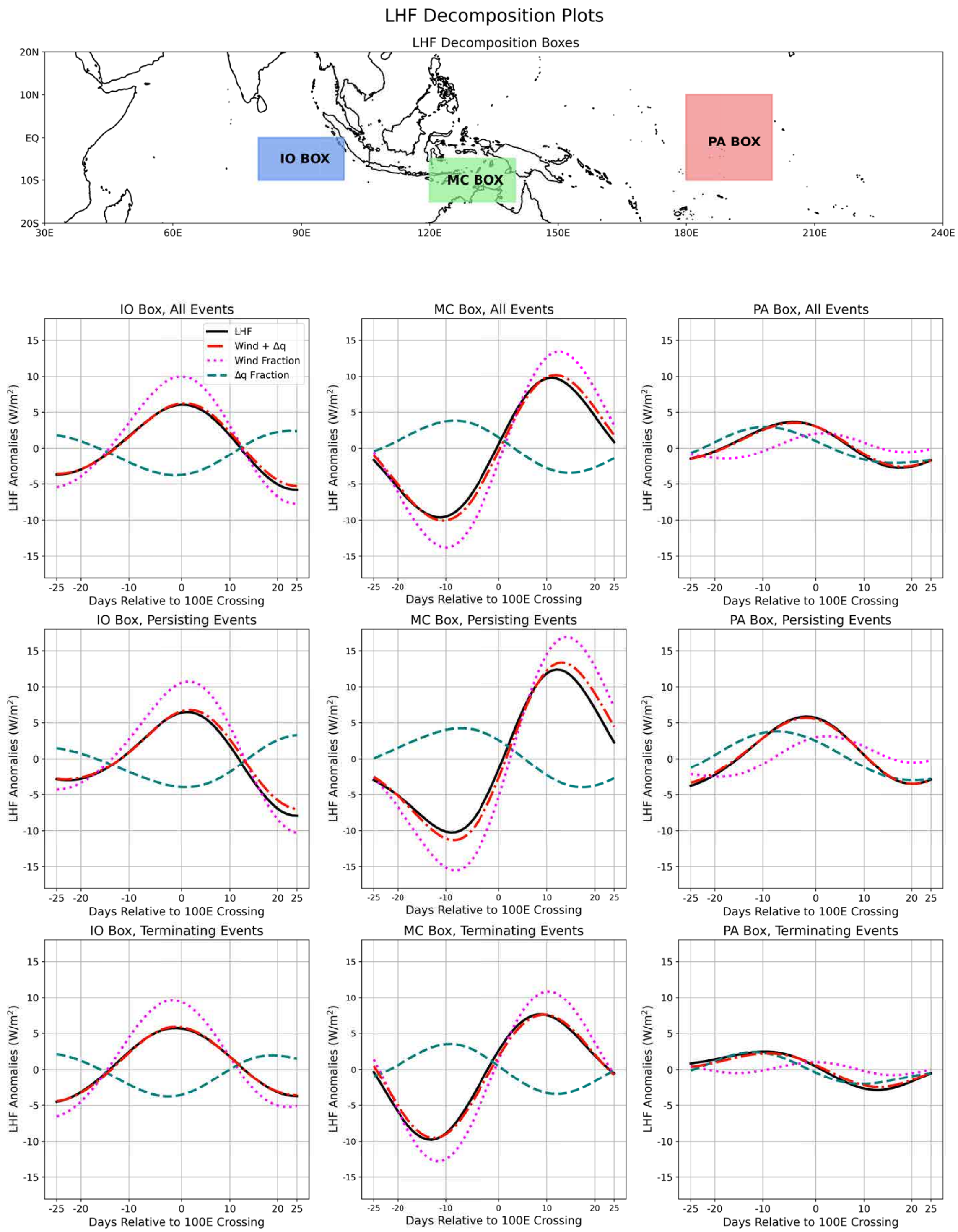

Figure 18: LHF decomposition across composite event lifetimes for the three regions shown in the top map. We see that in the IO and the MC LHF is primarily wind-driven with thermodynamic effects opposing dynamic effects. In the PA box for persisting events LHF is equally driven by thermodynamic and dynamic effects and of a similar scale to the LHF anomalies in the IO box.

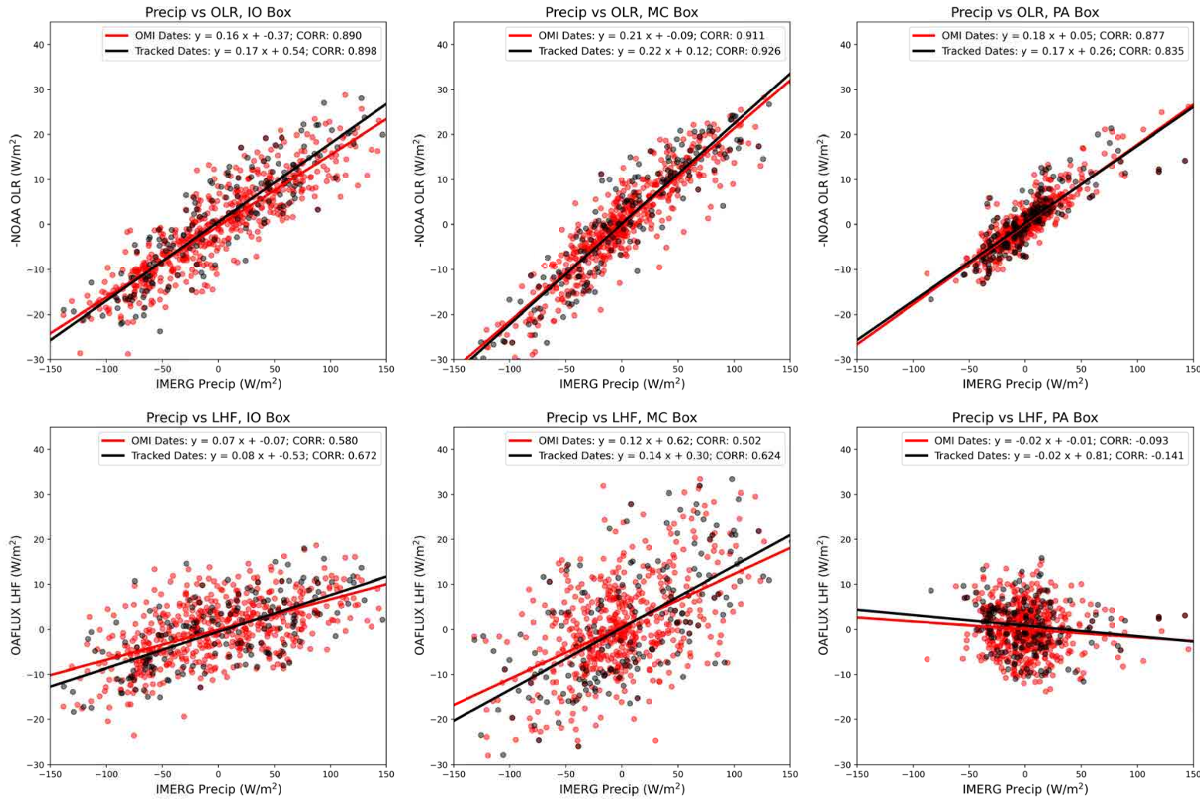

Figure 19: Relationship of MJO related variables in the three boxes used in Figure 18. For purposes of comparison IMERG precipitation has been expressed in W/m^2. In the IO and MC boxes the relationship between precipitation and LHF agrees with previous observations for MJO driven fluxes yet over the PA box this relationship is entirely absent.

For the IO and MC boxes we see that LHF has a correlation coefficient of 0.502-0.672 with precipitation, for both boxes our tracking algorithm produces a much stronger correlation with precipitation than the OMI index dates. These correlation coefficients agree with the results of Riley Dellaripa and Maloney (2015), and are just slightly below the reported values of Bui et al. (2020). More importantly, we can see that our LHF is also 7-14% the scale of precipitation in these boxes, which agrees with previous findings, and suggests that latent heat flux anomalies play an important role in helping to maintain MJO convection in the Maritime Continent region in the context of moisture mode theory. In comparison, column longwave radiative flux anomalies as diagnosed by negative OLR anomalies are about 16-21% of precipitation anomalies. In the PA Box however the correlation between LHF and local precipitation on MJO timescales is very small, with values of 0.093 and 0.141 and LHF is roughly 2% the scale of precipitation. This is a colder SST region with generally small intraseasonal precipitation anomalies, and this region is likely not a strong driver of MJO dynamics.

3.2 CYGNSS Results:

The CYclone Global Navigation Satellite System (CYGNSS) represents a new way to study tropical air-sea interactions in higher detail than before. Utilizing reflected Global Positioning System (GPS) signals off the ocean surface, CYGNSS retrieves ocean surface roughness to estimate surface winds and, with complementary reanalysis estimates of near-surface temperatures and humidity, latent heat flux. This allows CYGNSS to provide high quality hourly coverage for swaths of the tropical oceans. Because CYGNSS launched in late 2016 and scientific quality data began in 2018, the time span to study MJO events since the beginning of the CYGNSS region, while growing, is limited. However, we use the CYGNSS output that is available to provide a comparison to OAFLUX-derived results.

To make the most use of CYGNSS to provide a second observational look at MJO propagation we ran our tracking algorithm once more over the NOAA interpolated OLR dataset with a different convective identification threshold to maximize sample size. The binary map OLR anomaly threshold was changed from -15 W/m^2 to -10 W/m^2, the size threshold was changed from 10 pixels to 5 pixels, the number of frames over which the algorithm would search for a potential matching blob was increased to 15, and the requirement for a blob to be considered a continuation of previous identified blob was reduced from lasting 10 frames to lasting 2 frames.

For the two boreal winters beginning in 2018 and 2019, these settings yielded 5 tracked events, of which 2 were classified as persisting, and 3 were terminating. Two of these events were also identified using the original more conservative settings. Figure 20 shows the tracks for the 5 events. As in Figures 2 and 4, the tracks are smoothed using a simple 5-day moving average. Three of the events detour south of the MC region, one event initiates in and propagates through the MC, and one event initiated to the north of the MC and dissipates around 135°E.

Figure 20: Trajectories for the five events tracked in 2018-2019 using the CYGNSS tracking parameters.

Because the sample size is too limited for meaningful composites, we looked at each individual event on day 0 relative to its crossing 100E (Figures 21,22). All of the events have elevated wind speeds over the equatorial Pacific. In Figure 22, the large-scale spatial distribution of CYGNSS LHF anomalies is examined. For this small subset of MJO events, both persisting events and one terminating event (event 4) have elevated LHF across the Pacific, including around the intersection of the equator and the Dateline. Events 3 and 4 have a similar spatial pattern for LHF and surface winds despite being a persisting and terminating event respectively. Because the LHF anomalies in event 4 are reduced relative to event 3 despite event 4 having relatively enhanced surface winds over the equatorial Pacific we see the importance of thermodynamic drivers of LHF over this region. This is further supported by the fact that all events have elevated winds over the equatorial Pacific despite only three having elevated LHFs and only two propagating through the MC. The small sample size of our CYGNSS events prevents any definitive statements from being made but the few results available do agree with what we find with OAFLUX.

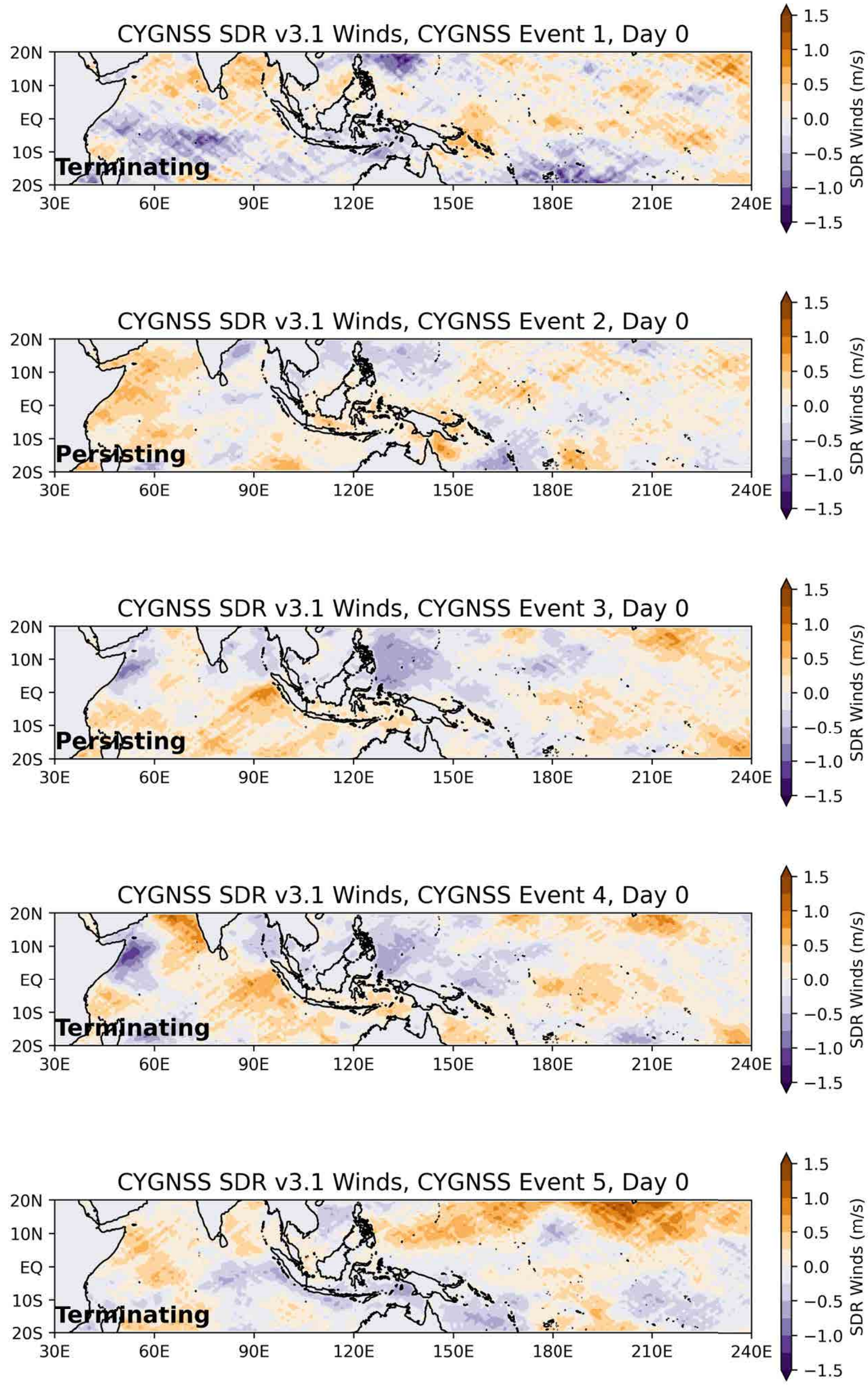

Figure 21: Plots of CYGNSS SDR v3.1 surface winds for the 5 CYGNSS events on day 0 relative to the centroid crossing 100°E. There are enhanced winds over the equatorial pacific for both persisting events and 2 out of 3 terminating events.

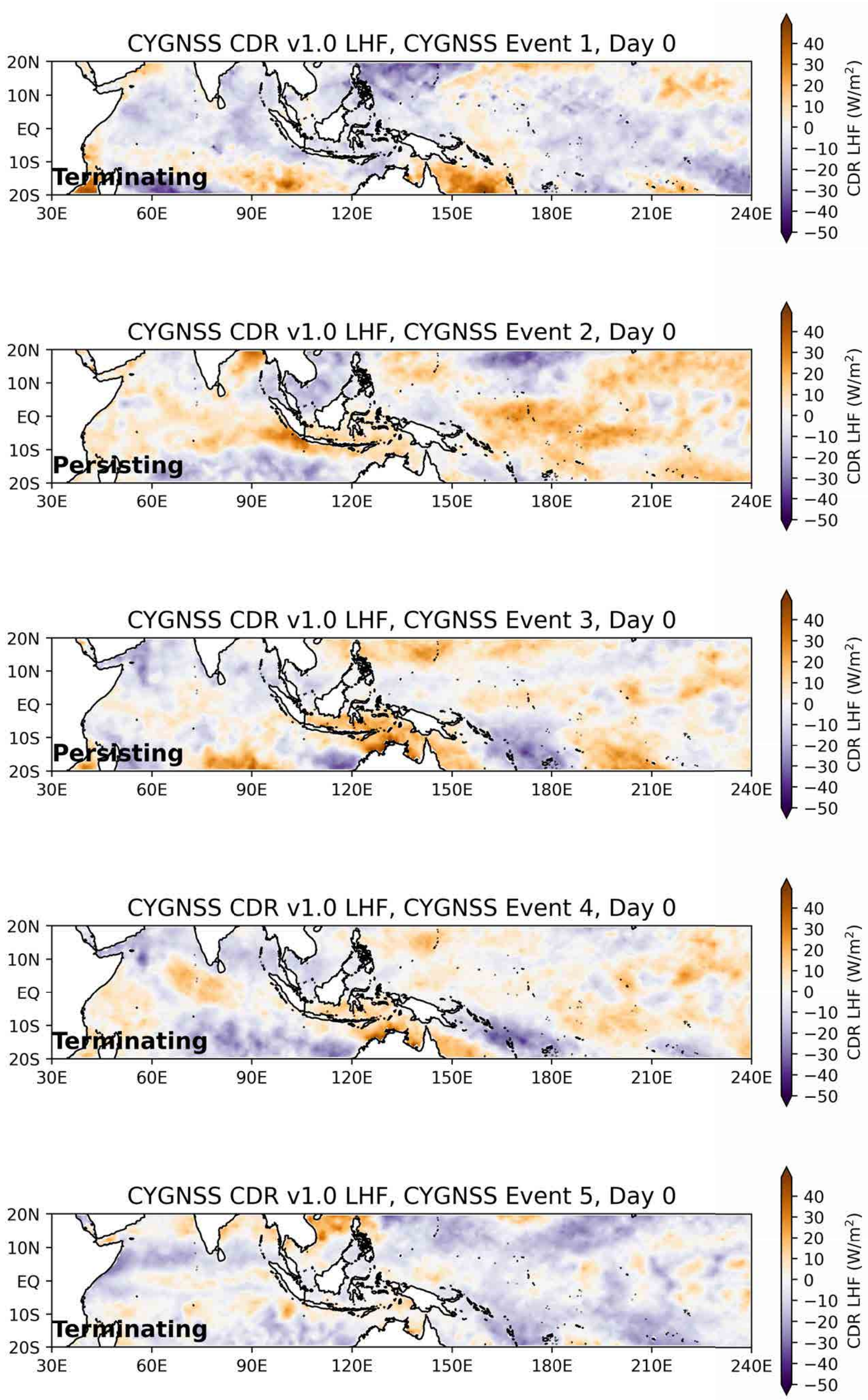

Figure 22: Similar to Figure 21 except CYGNSS CDR v1.0 LHF for the 5 CYGNSS events. The two persisting events (events 2 and 3) have elevated LHF across the Pacific Ocean. Event 4 shows a similar but reduced pattern despite being a terminating event.

3.3 Global Mean Wind:

In the work of Raymond and Fuchs (2017, 2018) and Sentić et al. (2020) an easterly low-level global mean wind in the tropics plays a key role in producing LHF for the MJO through WISHE. Using the long record of 1000 hPa zonal winds (the lowest pressure level available) provided by ERA5 we looked at the patterns of low-level global mean wind averaged from 10°N-10°S from 1979-2020 across the global tropics as they relate to propagating versus terminating events.

Figure 23 presents daily-mean zonal-wind averaged across the global tropics (0-360°E, 10°N-10°S) from 1979-2020. We see that the mean zonal wind across the entire year is easterly and is at its strongest during the period we defined 'boreal winter', December-April in particular, which is also when MJO amplitude maximizes. Figure 24 shows how the low-level background wind differs during persisting and terminating events. To do this, a meridional mean of the total 1000 hPa zonal wind from 10°N-10°S at each longitude was constructed for every day of tracking for both persisting (n = 1070 days) and terminating events (n = 687 days), producing a composite total winds for each event category. Over the Indian Ocean zonal mean wind for terminating events is westerly and has a maximum velocity of 1.5 m/s. For persisting events the mean wind speed is closer to zero with locations where it rises to 0.75 m/s. Over the Pacific Ocean from 150°E-215°E terminating events have a stronger easterly flow than persisting events by approximately 0.33 m/s. For both regions the differences are statistically significant at the 95% level using a two-sample T-test. To better isolate the mean background winds for persisting and terminating events we took the average of surface winds across the tropics starting 30 days before tracking initiated for each event until 30 days after tracking ceased for an event, lengthening the period of interest by 60 days for each event. For persisting events this results in a mean zonal wind speed of -2.89 m/s, and for terminating events -3.16 m/s, the difference between these two means is significant at the 95% level using a two-sample T-test.

This represents a further departure from the work of Raymond and Fuchs (2017,2018) because near the intersection of the Dateline and equator over the Pacific, where persisting events have the large-scale positive LHF anomaly that is absent from terminating events, terminating events have stronger easterlies. Terminating events also form in environments with stronger global low-level easterlies in the tropics. Given our results in Figure 18 showing the importance of a thermodynamic component in generating LHF over this region shows that a pure WISHE theory, while predicting this LHF region, does not fully explain its origins since LHF is reduced for events with stronger low-level background easterlies.

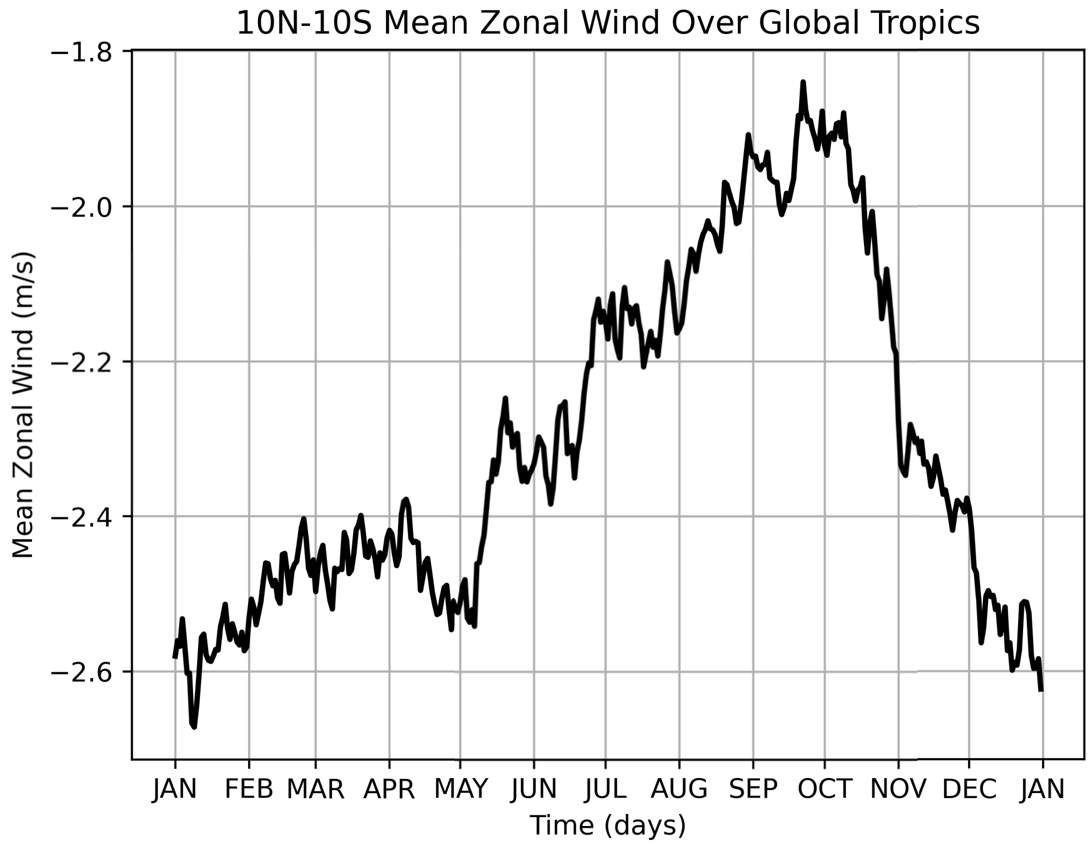

Figure 23: Daily Mean Global Zonal wind at 1000 hPa between 10°N-10°S across the globe (0-360°E) from ERA5 reanalysis from 1979-2020. The tropics have mean easterlies year round with the intensity of the easterlies peaking during 'boreal winter'.

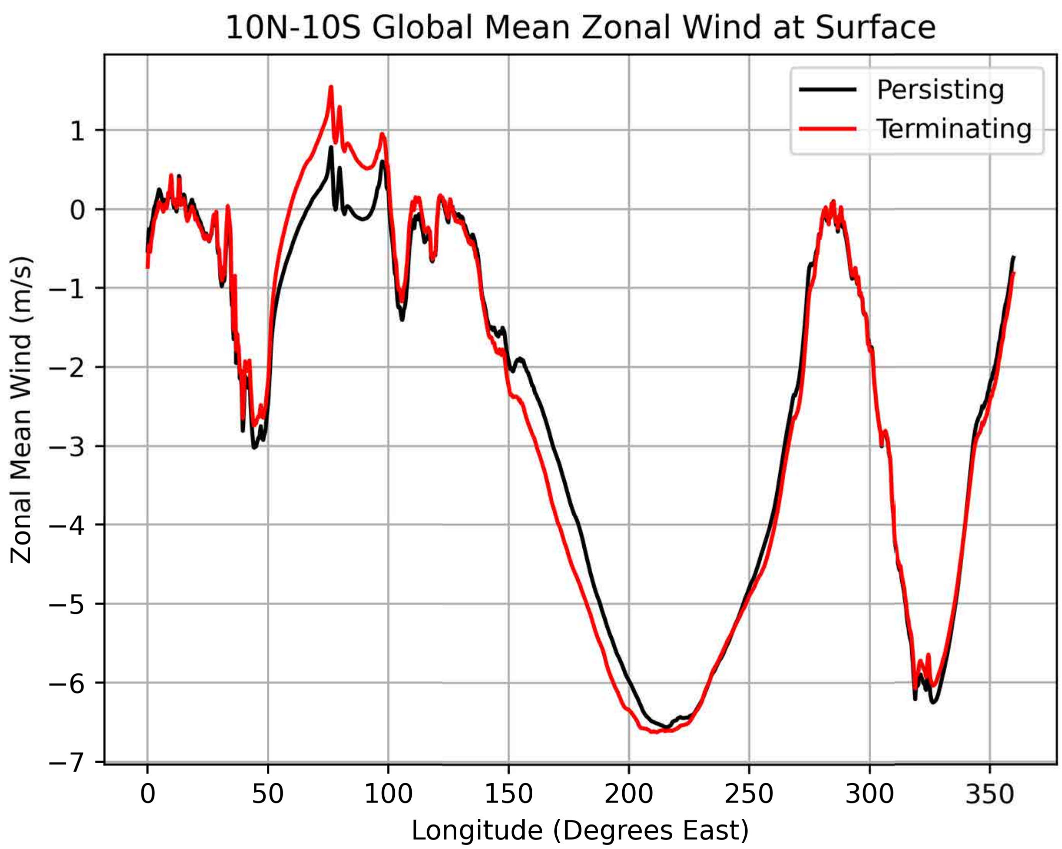

Figure 24: Composite global mean zonal wind from 10°N-10°S on days where our algorithm tracked persisting events (black) and terminating events (red). Terminating winds have stronger westerly winds over the Indian Ocean and stronger easterly winds over the Pacific Ocean compared to persisting events.

4 CESM2 Results

The tracking algorithm developed here also has applications for examining how MJO propagation characteristics may change in a future warmer climate. For example, previous studies have hypothesized that the MJO may travel further eastward with climate warming, increase in propagation speed, and potentially become more frequent (e.g. Maloney et al. 2019). Given that the NCAR CESM2 produces a good simulation of the MJO (Ahn et al. 2020; Danabasoglu et al. 2020), application of our tracking algorithm to this model provides an excellent opportunity to test some of these hypotheses.

Using the methodology outlined in section 2.3 we applied our tracking algorithm to 30-96 day band-pass filtered daily OLR anomalies from 6 different CESM2 experiments: SSP 2-4.5 (r1i1p1f1), SSP 5-8.5 (r1i1p1f1), 1% CO2 Increase per year until 4x CO_2 (r1i1p1f1), Abrupt 4xCO2 (r1i1p1f1), and 2 historical runs (r1i1p1f1, r10i1p1f1). Monthly near-surface temperature data was also acquired for the 6 CESM2 experiments.

The specific quantity that we compare between different global mean temperature regimes in the various CESM2 experiments is the propagation speed of those events. We seek to test the hypothesis that MJO events propagate faster as the Earth warms. To answer this hypothesis, starting with year 1 of each experiment, we partitioned the model data into ten year chunks. For each ten year chunk, we calculated the 10-year global mean near surface temperature and the mean propagation speed of tracked MJO events in that ten-year span. This was done across all 6 experiments and the results are plotted in Figure 25. A clear trend exists of increasing propagation speed with 10-year global mean near-surface temperature, with the events above 298K at their lowest speeds matching the highest speeds of events in the histr10 simulation. The best fit line yields a slope of approximately 0.036 (m/s)/k. So while this is not a large increase, it is notable across the range of temperatures present. The speed-up of MJO propagation speed with warming is consistent with results in prior studies (e.g. Bui and Maloney, 2020).

We next compared the distributions of event propagation speeds within each experiment to see how the distributions change (Figure 26). All of the simulation events are producing similar distributions in event speed with a slightly skewed right and approximately normal distribution. The mean speed of events in the abrupt 4xCO_2 simulation are noticeably higher than those of other simulations. The mean speeds for all 6 experiments are slower than that of the observational tracking results.

To test for statistical significance, we split all MJO events into three groups. MJO events that occurred when global mean near-surface temperature was less than 288K, between 288K and 295K, and above 295K. These divides were chosen because most historical events lie below 288K and the bulk of 4x

CO_2 events above 295K. We then used a two sample T-test to compare the distributions between the groups (Figure 27). The differences between each group were assessed to be statistically significant at the 95% level. Between the less than 280K and greater than 285K groups, this represents an increase of up to 2.5-5% in propagation speed for each degree of warming. This rate of propagation speed increase is consistent with that found by Adames et al. (2017) for the NASA GISS model, who showed a 3.3% increase in phase speed per degree warming. Hence, under a potential warming scenario of 2 degrees, it is possible that MJO events could speed up by 0.25 - 0.5 m/s.

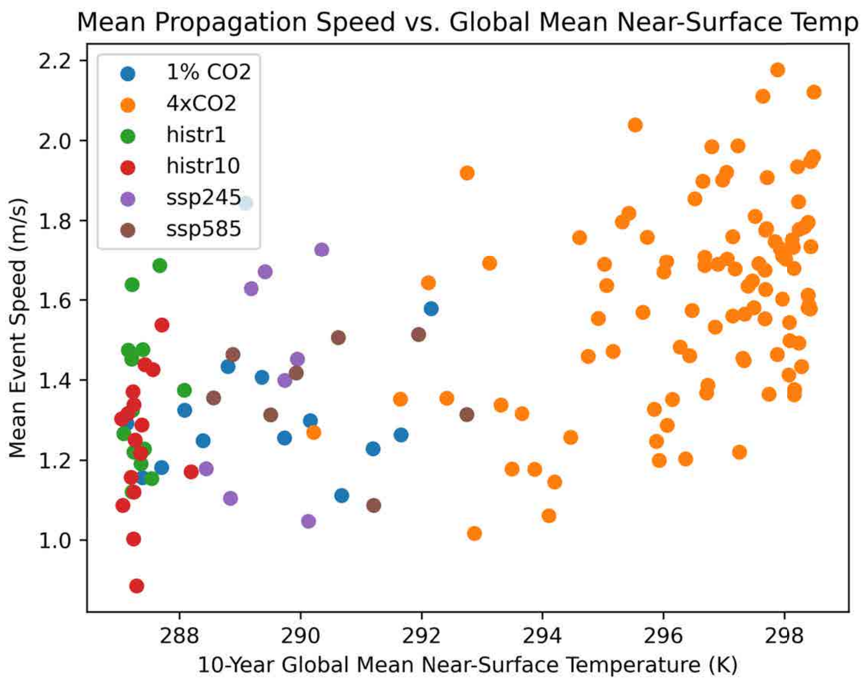

Figure 25: Relationship between mean event propagation speed and 10-year global mean near surface temperature for the 6 CESM2 experiments. There is an obvious positive relationship between the two quantities.

In Figures 28-33, tracking results are examined for each individual experiment, including starting longitude, ending longitude, and event length. For all 6 experiments the longitude where tracking ceased (ending longitude) doesn't have the same bimodal distribution as seen in the observational results. Instead the distribution appears to be centered around 150°E, the dividing line we used between persisting and terminating events. It appears that CESM2 may not be properly simulating the 'barrier effect' of the MC. While a proper investigation of this phenomena is outside the scope of this study, a deep dive into the differences between CESM2 and observations surrounding MJO propagation through the MC could prove invaluable to improving the next generation of climate models and improving MJO theory. One other finding that is apparent from comparing distributions across models is that MJO events in warmer climates propagate further east than those in control climates. This is apparent, for example, by comparing the ending longitude distributions for historical simulations (Figure 30 and 31) and RCP5-8.5 (Figure 33).

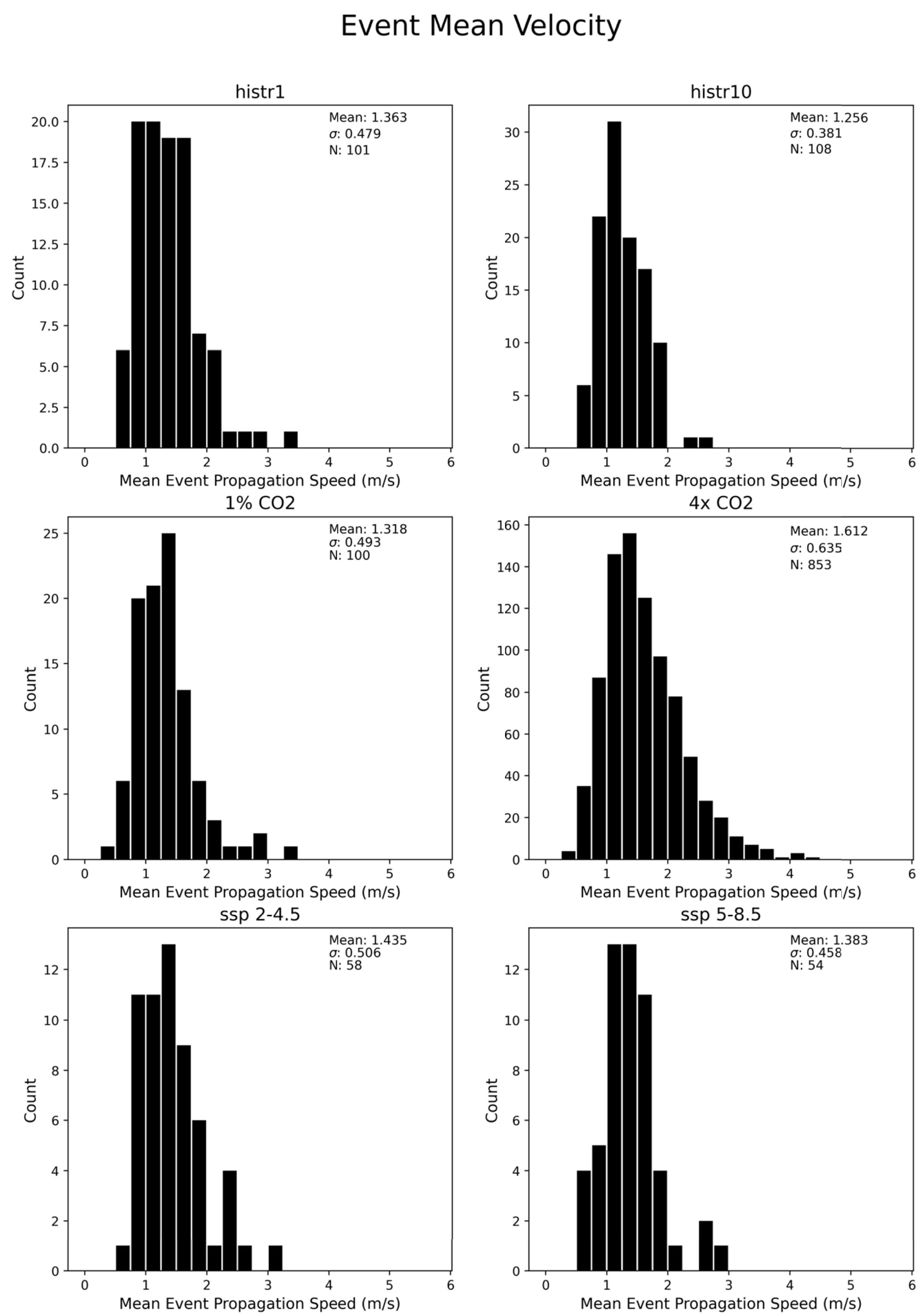

Figure 26: Distributions for event mean velocity for the 6 CESM2 experiments. We see that the abrupt 4x CO_2 experiment has events that on average propagation speed roughly 20-30% faster than the other experiments.

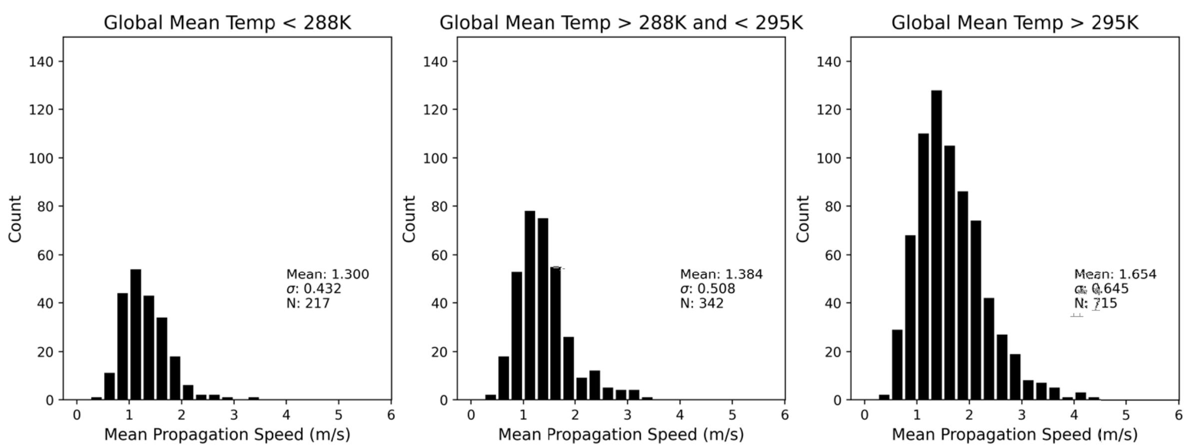

Figure 27: Distributions mean propagation speed for MJO events tracked for the 6 CESM2 experiments grouped by 10-year global mean near surface temperature. The increase in mean between the groups is statistically significant at the 95% level using a two-sample T-test.

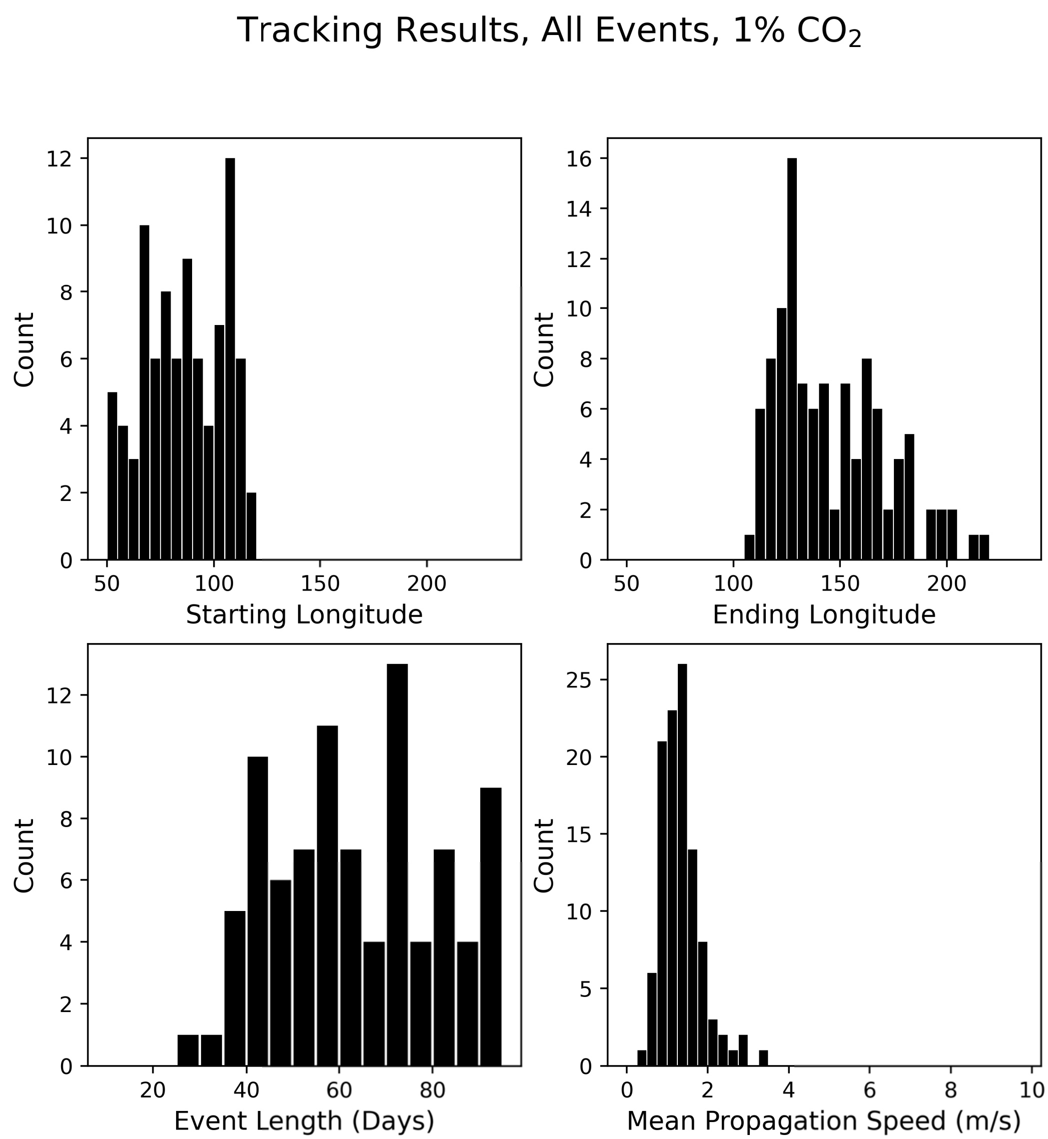

Figure 28: Similar to Figure 3 except for the 1% increase per in CO2 concentration per year CESM2 experiment.

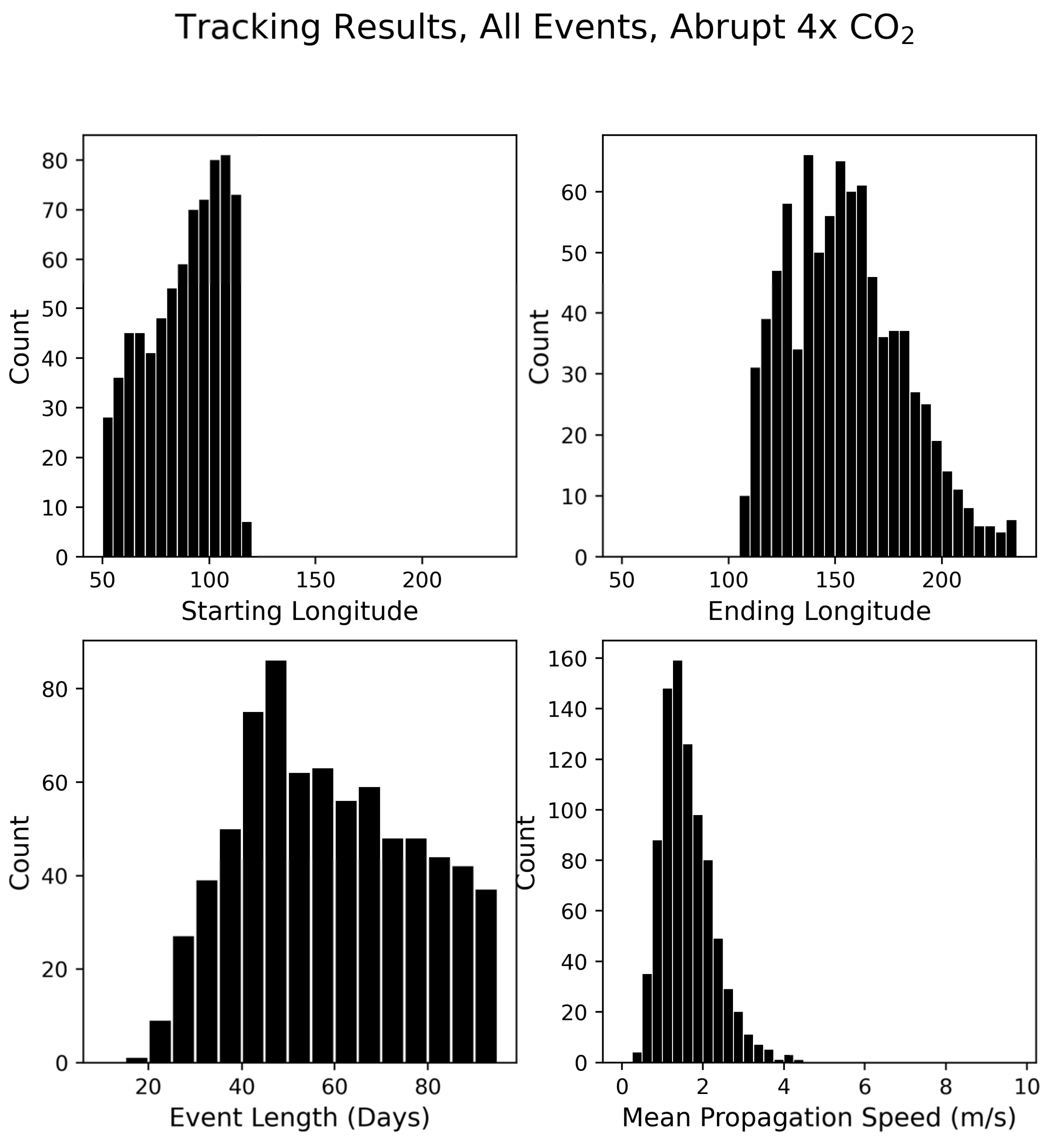

Figure 29: Similar to Figure 3 except for the abrupt 4x CO_2 CESM2 experiment.

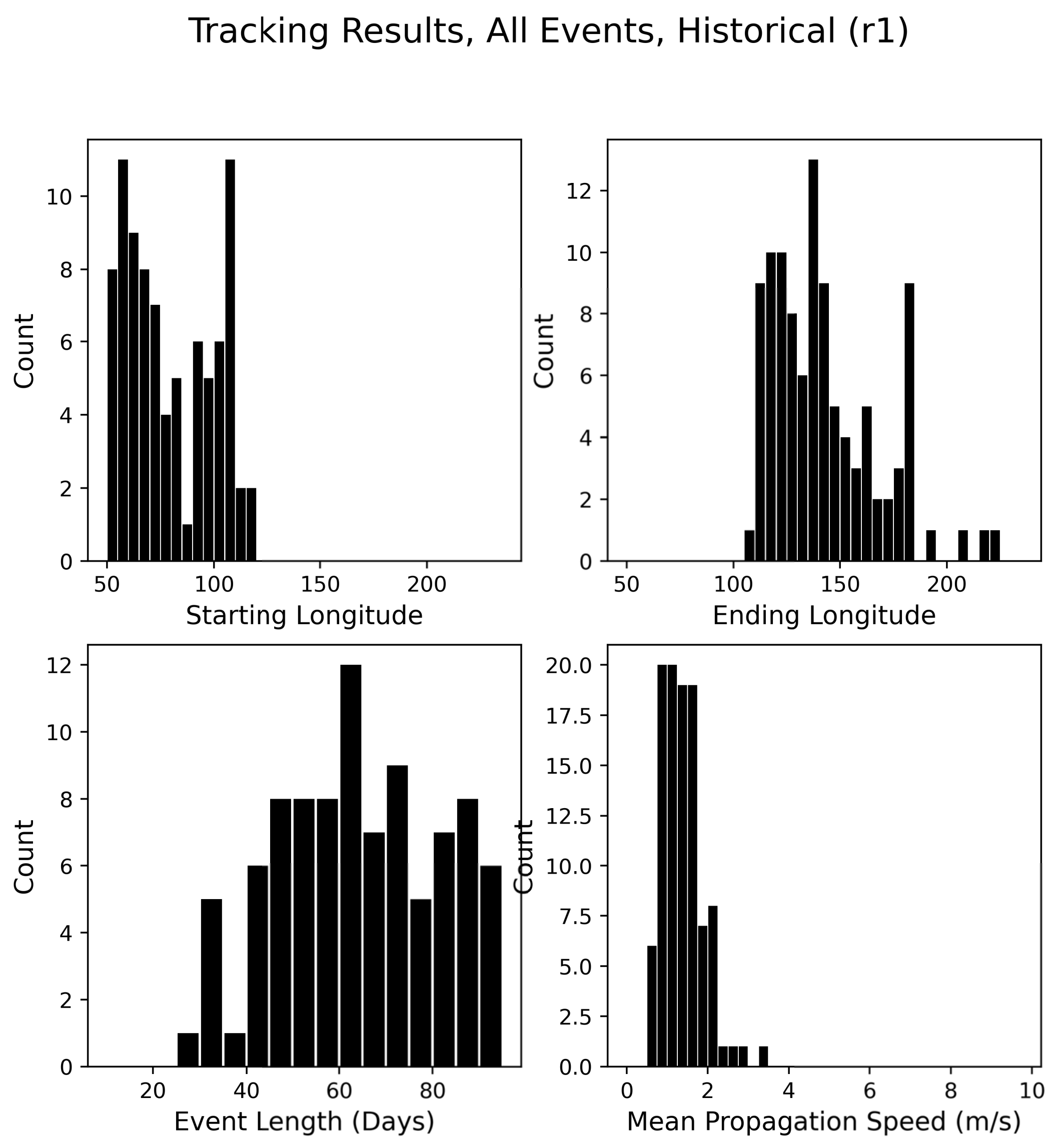

Figure 30: Similar to Figure 3 except for the realization 1 historical CESM2 experiment.

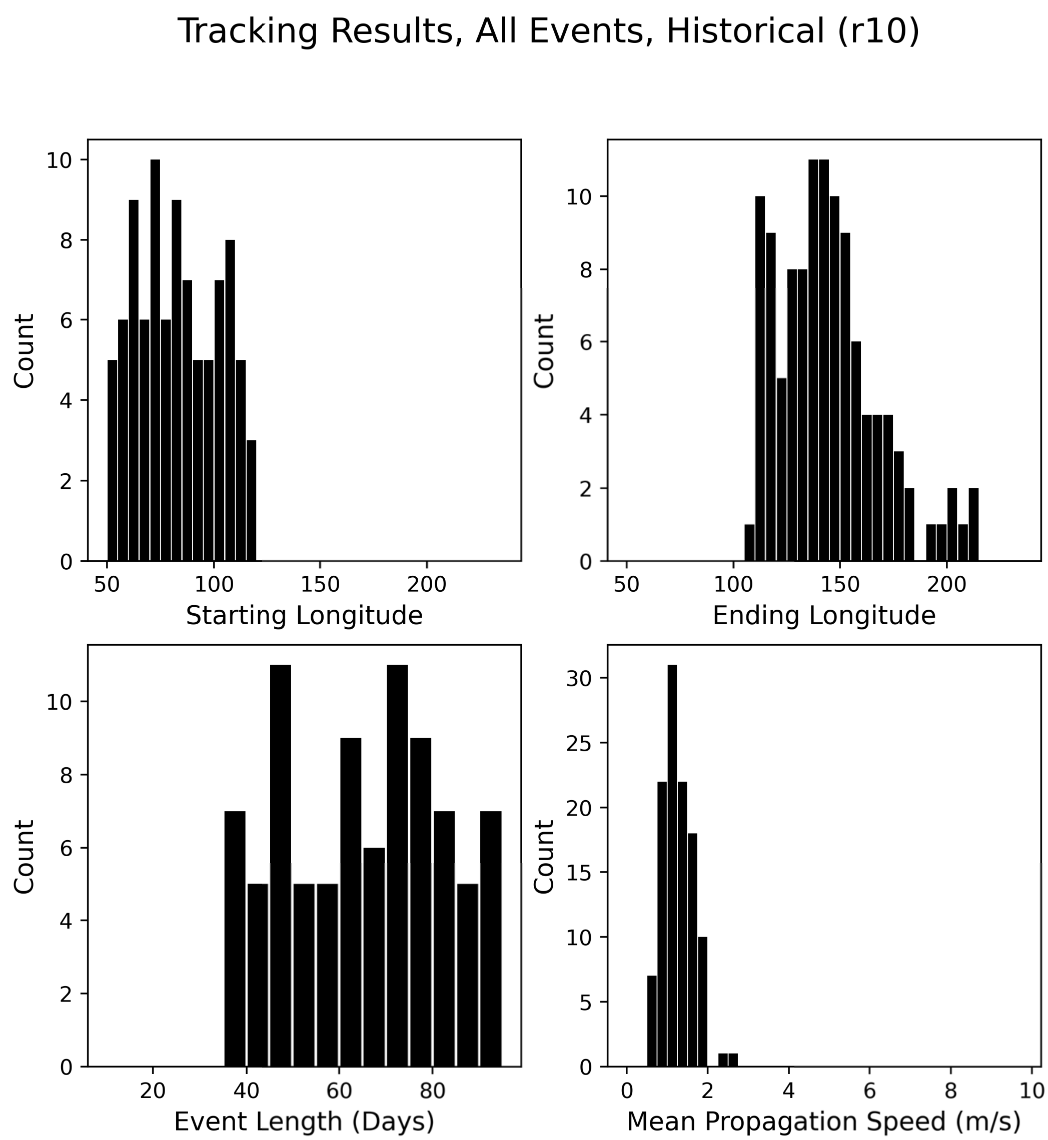

Figure 31: Similar to Figure 3 except for the realization 10 historical CESM2 experiment.

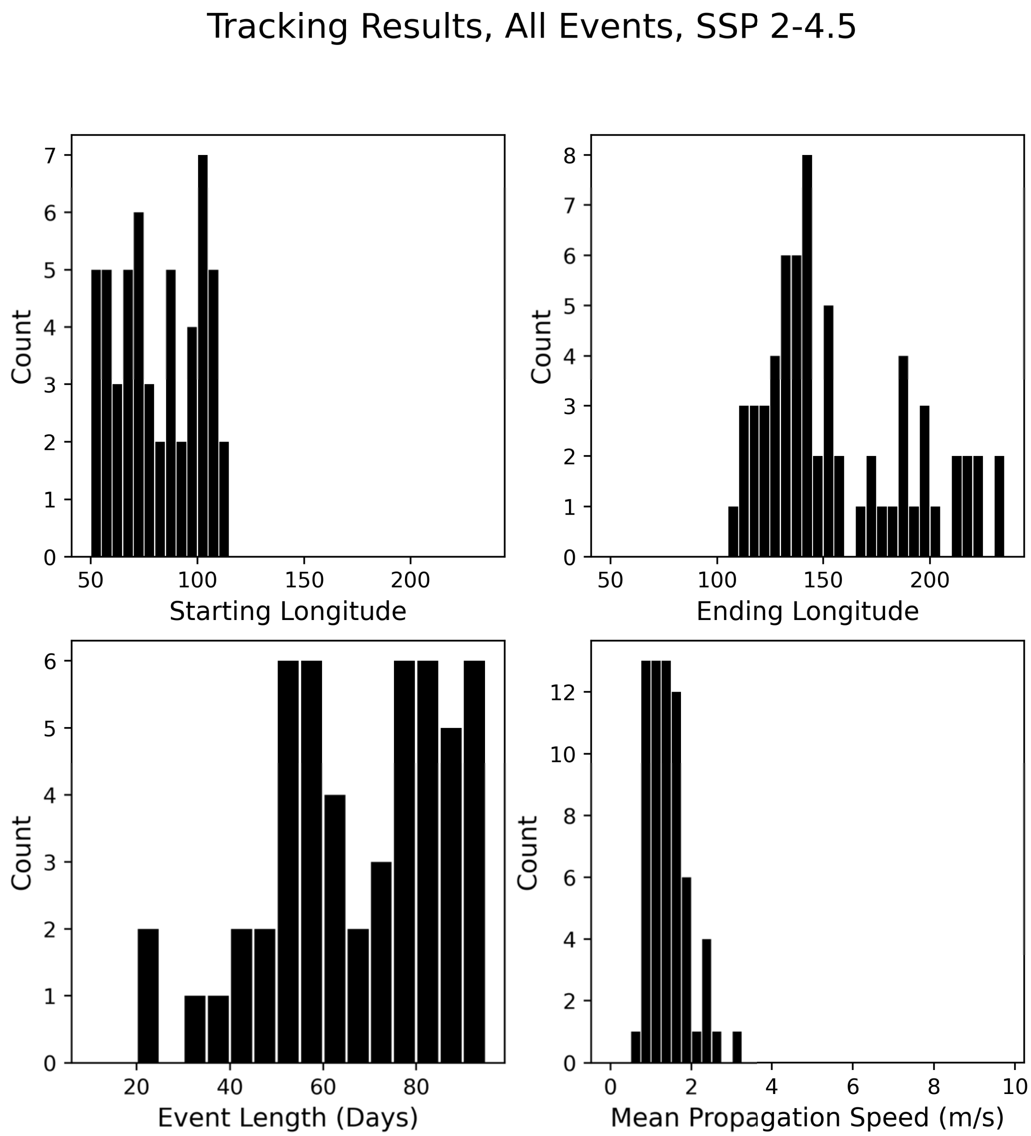

Figure 32: Similar to Figure 3 except for the SSP 2-4.5 CESM2 experiment.

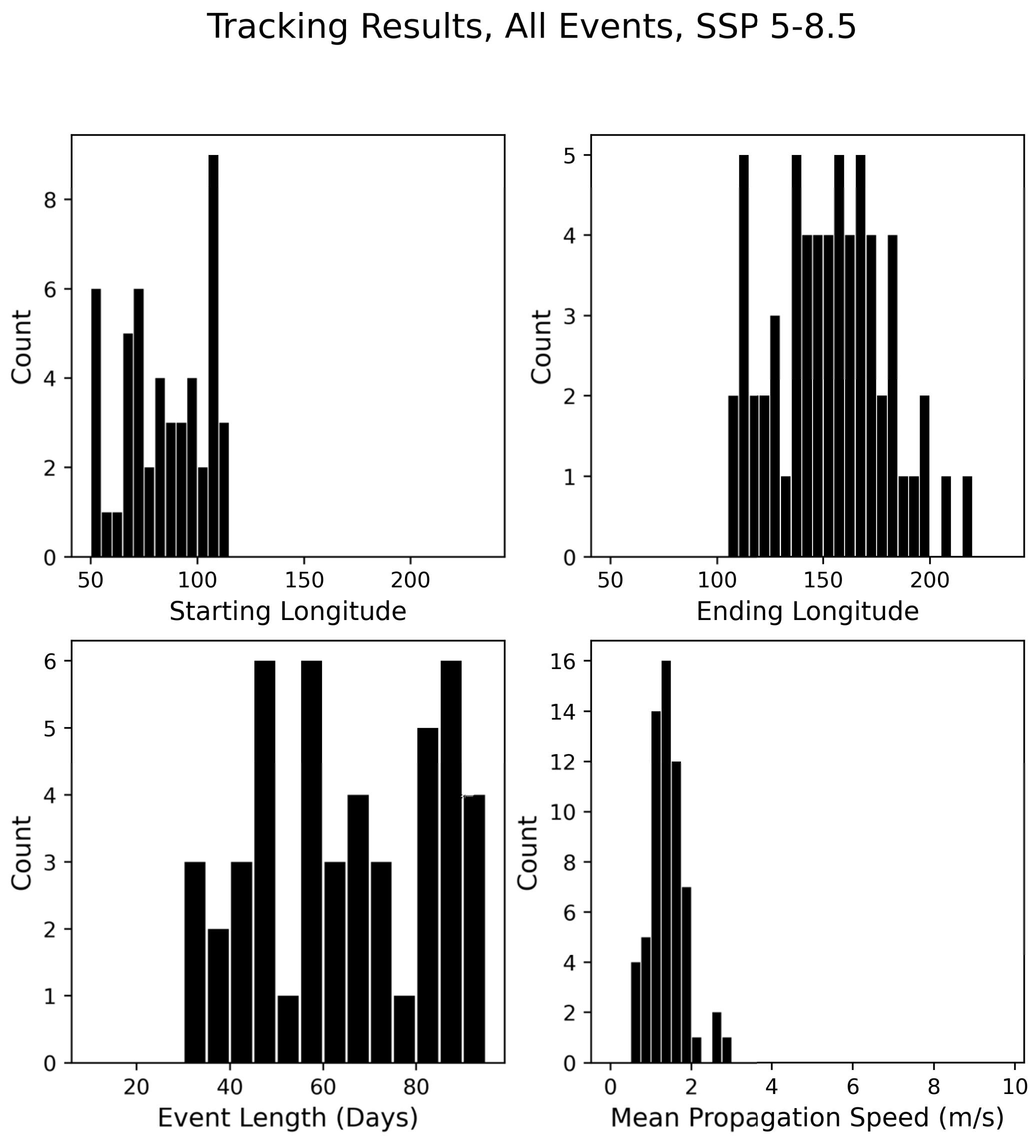

Figure 33: Similar to Figure 3 except for the SSP 5-8.5 CESM2 experiment.

5 Discussion

The results of Section 3 are used to test the importance of surface flux feedbacks to the MJO in the context of two major theories for MJO dynamics, moisture mode theory (e.g. Sobel and Maloney 2012; 2013), and WISHE (e.g. Raymond and Fuchs 2018). This study joins the body of recent theoretical, observational, and modeling studies have sought to understand the role of LHF in MJO maintenance and propagation (Bui et al., 2020; DeMott et al., 2014; DeMott et al., 2015; Emanuel, 2020; Fuchs and Raymond, 2017; Khairoutdinov and Emanuel 2018; Maloney, 2009; Raymond and Fuchs, 2018; Riley Dellaripa and Maloney, 2015; Sentić et al., 2020; Sobel and Maloney, 2012; Wolding and Maloney, 2015). Regarding WISHE theory, in section 3 we showed that there is a quasi-stationary positive intraseasonal LHF anomaly over the equatorial Pacific Ocean centered around 180°E-200°E that is present for events that persist through the MC region and absent for those that terminate over that region. WISHE theories to explain MJO propagation produce results that agree with our observations, at least in terms of the presence of this latent heat flux signal; however the enhanced fluxes that contribute to the production of moisture east of the MJO are not entirely wind-driven in our observations, and this does represent a discrepancy between our results and recent theory.

Sentić et al. (2020) expounds upon the ideas presented in Fuchs and Raymond (2017) and Raymond and Fuchs (2018) by examining a composite MJO event from reanalysis. In their analysis, they found that there is a large, slow-moving positive LHF anomaly to the east of the center of MJO convection. This is similar to the phenomena we identified in our study that is centered around 180°E-200°E. The flux feature in their study is associated with a moistening of the boundary layer, although their observed LHF anomalies are slightly displaced in space and time relative to the boundary layer moistening, with the moistening signal occurring west of the LHF anomaly and east of the center of MJO convection. Our results further diverge from these ideas in that over this region terminating events have increased background easterly winds compared to persisting events despite producing less LHF.

Arnold and Randall (2015) as well as Khairoutdinov and Emanuel (2018) present a convective self-aggregation model of an MJO-like disturbance that produces similar features to observed events. Both studies produce a peak in surface fluxes and moisture advection to the east of MJO convection that roughly aligns with where our observations place the LHF anomaly. We note, however, that those studies are conducted using zonally-symmetric aquaplanets in which mean easterly winds are located everywhere in the tropics, unlike the real world where regions of mean westerlies exist in the Indo-Pacific warm pool (Maloney and Sobel 2004).

Our results show that the leading LHF anomaly over the equatorial Pacific is driven equally by dynamic and thermodynamic effects. If this flux anomaly over the Central Pacific is essential to MJO propagation, it suggests that an entirely wind-driven theory for LHF propagation may be insufficient and some thermodynamic mechanism could be needed to complete the explanation. We also show that our observed LHF anomaly over the Pacific does not have a noticeable phase speed in a Hovmöller composite. This suggests that the driver of this anomaly differs in detail from that in papers like Raymond and Fuchs (2018) where the latent heat flux anomaly to the east of MJO convection propagates eastward more continuously. The fast MJO circulation propagation away from the west Pacific that imposes same-signed wind anomalies across the east Pacific may impose this feature (e.g. Rydbeck et al. 2013), or a temporary phase alignment of multiple processes may cause this behavior. We also see that for events that fail to propagate through the MC the mean low-level easterly winds are slightly enhanced compared to those that propagate through the region, suggesting further refinement to WISHE theories may be needed.

6 Conclusions

We present a new algorithm that is capable of identifying and tracking MJO events using 30-96 day bandpass filtered OLR anomalies. This algorithm is capable of tracking multiple events at once and leverages the effects of a bandpass filter to reduce computational cost. This technique is first applied to track MJO events using NOAA interpolated OLR anomalies from 1985-2019, before examining MJO tracks in the NCAR CESM2 in current and a warmer climate. Using this algorithm we investigated the role of fluxes both locally and globally in MJO propagation.

We found 36 MJO events and 50% of them fail to propagate through the MC region. Most events, whether they terminate over the MC or not, detour to the south of the MC which agrees with previous observational results. We find that persisting events have a stronger and more coherent LHF signal compared to terminating events over every phase of the MJO despite similar composite ratios of LHF and OLR anomalies to precipitation for both categories of events. We also find that terminating events tend to be smaller in scale, consistent with previous results in the literature that indicated MJO events with larger spatial scales are better able to propagate eastward.

We also find that for events that propagate through the MC, a large stationary region of positive LHF over the central and eastern equatorial Pacific is present that is absent for terminating events. While the presence of this feature is broadly consistent with modern theories of MJO propagation involving WISHE, it is stationary and has a large thermodynamic component in addition to a wind component, feature,, making the details different from that predicted in the work of Fuchs and Raymond (2017) and Raymond and Fuchs (2018). A modified thermodynamic component in addition to WISHE may be needed to fully understand how these positive LHF anomalies help MJO events overcome the 'barrier effect' of the MC. We also find that events that fail to propagate through the MC have stronger background low-level easterly winds across the tropical Pacific, a feature that should support their propagation through the MC in WISHE model, although is lacking here.

Applying our tracking algorithm to 6 different CESM2 experiments we found that MJO propagation speed has a statistically significant positive relationship with 10-year mean global surface temperature. MJO events increase in propagation speed between 2.5-5% per degree of warming. These results are consistent with previous research that predicts an increase in MJO propagation speed with global warming. We also found that the CESM2 experiments did not reproduce the observed bimodal effect in MJO termination longitude that is seen in observations due to the 'barrier effect' of the MC.

Future work from this study will focus on investigating differences between CESM2 and observations to both understand how to improve CESM2's simulation of the MJO and understand what possible key features are necessary to produce a MC 'barrier effect.' Other avenues for future work are investigating the intensity and importance of moisture advection from the anomalous Pacific Ocean LHF region towards the MJO, the mechanisms that form this region of high LHF across the equatorial Pacific, and looking at global wind anomalies for propagating and terminating events to understand the scale of intensity of dynamical signals associated with spatially larger convective anomalies. As more CYGNSS data becomes available, it will be possible to examine LHF anomalies of future MJO events in enhanced detail possibly providing more clues into how LHF impacts MJO propagation.

7 References

1.

Adames, Á. F. & Kim, D. The MJO as a Dispersive, Convectively Coupled Moisture Wave: Theory and Observations. Journal of the Atmospheric Sciences 73, 913–941 (2016).

2.

Adames, Á. F., Kim, D., Sobel, A. H., Del Genio, A. & Wu, J. Changes in the structure and propagation of the M JO with increasing C O 2. J. Adv. Model. Earth Syst. 9, 1251–1268 (2017).

3.

Afroosa, M. et al. Madden-Julian oscillation winds excite an intraseasonal see-saw of ocean mass that affects Earth's polar motion. Commun Earth Environ 2, 139 (2021).

4.

Ahn, M. et al. MJO Propagation Across the Maritime Continent: Are CMIP6 Models Better Than CMIP5 Models? Geophys. Res. Lett. 47, (2020).

5.

Araligidad, N. M. & Maloney, E. D. Wind-driven latent heat flux and the intraseasonal oscillation. Geophys. Res. Lett. 35, L04815 (2008).

6.

Arcodia, M. C., Kirtman, B. P. & Siqueira, L. S. P. How MJO Teleconnections and ENSO Interference Impacts U.S. Precipitation. Journal of Climate 33, 4621–4640 (2020).

7.

Arnold, N. P. & Randall, D. A. Global-scale convective aggregation: Implications for the Madden-Julian Oscillation: GLOBAL-SCALE CONVECTIVE AGGREGATION. J. Adv. Model. Earth Syst. 7, 1499–1518 (2015).

8.

Baggett, C. F., Barnes, E. A., Maloney, E. D. & Mundhenk, B. D. Advancing atmospheric river forecasts into subseasonal-to-seasonal time scales: Forecasting ARs at S2S Time Scales. Geophys. Res. Lett. 44, 7528–7536 (2017).

9.

Barnes, E. A., Samarasinghe, S. M., Ebert-Uphoff, I. & Furtado, J. C. Tropospheric and Stratospheric Causal Pathways Between the MJO and NAO. J. Geophys. Res. Atmos. 124, 9356–9371 (2019).

10.

Bui, H. X. & Maloney, E. D. Changes to the Madden-Julian Oscillation in Coupled and Uncoupled Aquaplanet Simulations With 4xCO 2. J. Adv. Model. Earth Syst. 12, (2020).

11.

Bui, H. X., Maloney, E. D., Riley Dellaripa, E. M. & Singh, B. Wind Speed, Surface Flux, and Intraseasonal Convection Coupling From CYGNSS Data. Geophys. Res. Lett. 47, (2020).

12.

CLIVAR MADDEN-JULIAN OSCILLATION WORKING GROUP. MJO Simulation Diagnostics. Journal of Climate 22, 3006–3030 (2009).

13.

Copernicus Climate Change Service (C3S) (2017). ERA5: Fifth Generation of ECMWF atmospheric reanalyses of the global climate. Copernicus Climate Change Service Climate Data Store (CDS), 1/5/2022. https://cds.climate.copernicus.eu/cdsapp#!/home.

14.

Crespo, J., Posselt, D. & Asharaf, S. CYGNSS Surface Heat Flux Product Development. Remote Sensing 11, 2294 (2019).

15. Danabasoglu, G. et al. The Community Earth System Model Version 2 (CESM2). J. Adv. Model. Earth Syst. 12, (2020).

16.

de Szoeke, S. P. & Maloney, E. D. Atmospheric Mixed Layer Convergence from Observed MJO Sea Surface Temperature Anomalies. Journal of Climate 33, 547–558 (2020).

17.

DeMott, C. A., Klingaman, N. P. & Woolnough, S. J. Atmosphere-ocean coupled processes in the Madden-Julian oscillation. Rev. Geophys. 53, 1099–1154 (2015).

18.

DeMott, C. A., Stan, C., Randall, D. A. & Branson, M. D. Intraseasonal Variability in Coupled GCMs: The Roles of Ocean Feedbacks and Model Physics. J. Climate 27, 4970–4995 (2014).

19.

DeMott, C. A., Wolding, B. O., Maloney, E. D. & Randall, D. A. Atmospheric Mechanisms for MJO Decay Over the Maritime Continent. J. Geophys. Res. Atmos. 123, 5188–5204 (2018).

20.

Emanuel, K. Slow Modes of the Equatorial Waveguide. Journal of the Atmospheric Sciences 77, 1575–1582 (2020).

21.

Emanuel, K. A. An Air-Sea Interaction Model of Intraseasonal Oscillations in the Tropics. J. Atmos. Sci. 44, 2324–2340 (1987).

22.

Fuchs, Ž. & Raymond, D. J. A simple model of intraseasonal oscillations. J. Adv. Model. Earth Syst. 9, 1195–1211 (2017).

23.

Gleason, S. et al. Characterizing and Mitigating Digital Sampling Effects on the CYGNSS Level 1 Calibration. IEEE Trans. Geosci. Remote Sensing 1–1 (2021) doi:10.1109/TGRS.2021.3120026.

24.

Gonzalez, A. O. & Jiang, X. Distinct Propagation Characteristics of Intraseasonal Variability Over the Tropical West Pacific. J. Geophys. Res. Atmos. 124, 5332–5351 (2019).

25.

Guan, B. & Waliser, D. E. Detection of atmospheric rivers: Evaluation and application of an algorithm for global studies: Detection of Atmospheric Rivers. J. Geophys. Res. Atmos. 120, 12514–12535 (2015).

26.

Hersbach, H. et al. The ERA5 global reanalysis. Q.J.R. Meteorol. Soc. 146, 1999–2049 (2020).

27.

Hirata, F. E., Webster, P. J. & Toma, V. E. Distinct manifestations of austral summer tropical intraseasonal oscillations: TROPICAL INTRASEASONAL OSCILLATIONS. Geophys. Res. Lett. 40, 3337–3341 (2013).

28.

Hsiao, W.-T. et al. Role of the Tropics and its Extratropical Teleconnections in State-Dependent Improvements of U.S. West Coast UFS Precipitation Forecasts.
http://www.essoar.org/doi/10.1002/essoar.10508184.1 (2022) doi:10.1002/essoar.10508184.1.

29.

Huffman, G. J., Stocker, E. F., Bolvin, D. T., Nelkin, E. J. & Tan, J. GPM IMERG Final Precipitation L3 1 day 0.1 degree x 0.1 degree V06. (2019) doi:10.5067/GPM/IMERGDF/DAY/06.

30.

Inness, P. M. & Slingo, J. M. The interaction of the Madden–Julian Oscillation with the Maritime Continent in a GCM. Q. J. R. Meteorol. Soc. 132, 1645–1667 (2006).

31.

Jiang, X. et al. Fifty Years of Research on the Madden-Julian Oscillation: Recent Progress, Challenges, and Perspectives. J. Geophys. Res. Atmos. 125, (2020).

32.

Jones, P. W. First- and Second-Order Conservative Remapping Schemes for Grids in Spherical Coordinates. Mon. Wea. Rev. 127, 2204–2210 (1999).

33.

Kerns, B. W. & Chen, S. S. Large-scale precipitation tracking and the MJO over the Maritime Continent and Indo-Pacific warm pool. J. Geophys. Res. Atmos. 121, 8755–8776 (2016).

34.

Kerns, B. W. & Chen, S. S. A 20-Year Climatology of Madden-Julian Oscillation Convection: Large-Scale Precipitation Tracking From TRMM-GPM Rainfall. J. Geophys. Res. Atmos. 125, (2020).

35.

Khairoutdinov, M. F. & Emanuel, K. Intraseasonal Variability in a Cloud-Permitting Near-Global Equatorial Aquaplanet Model. Journal of the Atmospheric Sciences 75, 4337–4355 (2018).

36.

Kiladis, G. N. et al. A Comparison of OLR and Circulation-Based Indices for Tracking the MJO. Monthly Weather Review 142, 1697–1715 (2014).

37.

Kim, D., Kug, J.-S. & Sobel, A. H. Propagating versus Nonpropagating Madden–Julian Oscillation Events. Journal of Climate 27, 111–125 (2014).

38.

Lee, H.-J. & Seo, K.-H. Impact of the Madden-Julian oscillation on Antarctic sea ice and its dynamical mechanism. Sci Rep 9, 10761 (2019).

39.

Liebmann, B. & Smith, C. A. Description of a Complete (Interpolated) Outgoing Longwave Radiation Dataset. Bulletin of the American Meteorological Society 77, 1275–1277 (1996).

40.

Ling, J. et al. Global versus Local MJO Forecast Skill of the ECMWF Model during DYNAMO. Monthly Weather Review 142, 2228–2247 (2014).

41.

Ling, J., Zhang, C., Joyce, R., Xie, P. & Chen, G. Possible Role of the Diurnal Cycle in Land Convection in the Barrier Effect on the MJO by the Maritime Continent. Geophys. Res. Lett. 46, 3001–3011 (2019).

42.

Madden, R. A. & Julian, P. R. Detection of a 40–50 Day Oscillation in the Zonal Wind in the Tropical Pacific. J. Atmos. Sci. 28, 702–708 (1971).

43.

Madden, R. A. & Julian, P. R. Description of Global-Scale Circulation Cells in the Tropics with a 40–50 Day Period. J. Atmos. Sci. 29, 1109–1123 (1972).

44.

Maloney, E. D. The Moist Static Energy Budget of a Composite Tropical Intraseasonal Oscillation in a Climate Model. Journal of Climate 22, 711–729 (2009).

45.

Maloney, E. D., Adames, Á. F. & Bui, H. X. Madden–Julian oscillation changes under anthropogenic warming. Nature Clim Change 9, 26–33 (2019).

46.

Maloney, E. D. & Esbensen, S. K. A Modeling Study of Summertime East Pacific Wind-Induced Ocean Atmosphere Exchange in the Intraseasonal Oscillation. Journal of Climate 18, 568–584 (2005).

47.

Maloney, E. D. & Hartmann, D. L. Modulation of Hurricane Activity in the Gulf of Mexico by the Madden-Julian Oscillation. Science 287, 2002–2004 (2000).

48.

Maloney, E. D. & Hartmann, D. L. Modulation of Eastern North Pacific Hurricanes by the Madden–Julian Oscillation. J. Climate 13, 1451–1460 (2000).

49.

Maloney, E. D. & Sobel, A. H. Surface Fluxes and Ocean Coupling in the Tropical Intraseasonal Oscillation. Journal of Climate 17, 4368–4386 (2004).

50.

McPhaden, M. J. Genesis and Evolution of the 1997-98 El Niño. Science 283, 950–954 (1999).

51.

Nardi, K. M. et al. Skillful All-Season S2S Prediction of U.S. Precipitation Using the MJO and QBO. Weather and Forecasting 35, 2179–2198 (2020).

52.

NASA/JPL. CYGNSS Level 2 Surface Flux Climate Data Record Version 1.1. (2020) doi:10.5067/CYGNS-C2H11.

53.

Neelin, J. D., Held, I. M. & Cook, K. H. Evaporation-Wind Feedback and Low-Frequency Variability in the Tropical Atmosphere. J. Atmos. Sci. 44, 2341–2348 (1987).

54.

Pascual, D., Clarizia, M. P. & Ruf, C. S. Improved CYGNSS Wind Speed Retrieval Using Significant Wave Height Correction. Remote Sensing 13, 4313 (2021).

55.

Raymond, D. J. & Fuchs, Ž. The Madden-Julian Oscillation and the Indo-Pacific Warm Pool. J. Adv. Model. Earth Syst. 10, 951–960 (2018).

56.

Riley Dellaripa, E. M. & Maloney, E. D. Analysis of MJO Wind-Flux Feedbacks in the Indian Ocean Using RAMA Buoy Observations. Journal of the Meteorological Society of Japan 93A, 1–20 (2015).

57.

Ruf, C. Cyclone Global Navigation Satellite System (CYGNSS) Algorithm Theoretical Basis Document Level 3 Gridded Wind Speed. (2018).

58.

Ruf, C. et al. In-Orbit Performance of the Constellation of CYGNSS Hurricane Satellites. Bulletin of the American Meteorological Society 100, 2009–2023 (2019).

59.

Ruf, C. S. et al. New Ocean Winds Satellite Mission to Probe Hurricanes and Tropical Convection. Bulletin of the American Meteorological Society 97, 385–395 (2016).

60.

Ruppert, J. H. & Johnson, R. H. Diurnally Modulated Cumulus Moistening in the Preonset Stage of the Madden–Julian Oscillation during DYNAMO*. Journal of the Atmospheric Sciences 72, 1622–1647 (2015).

61.

Rydbeck, A. V., Maloney, E. D., Xie, S.-P., Hafner, J. & Shaman, J. Remote Forcing versus Local Feedback of East Pacific Intraseasonal Variability during Boreal Summer. Journal of Climate 26, 3575–3596 (2013).

62.

Salby, M. L. & Hendon, H. H. Intraseasonal Behavior of Clouds, Temperature, and Motion in the Tropics. J. Atmos. Sci. 51, 2207–2224 (1994).

63.

Sentić, S., Fuchs-Stone, Ž. & Raymond, D. J. The Madden-Julian Oscillation and Mean Easterly Winds. J. Geophys. Res. Atmos. 125, (2020).

64.

Shi, X., Kim, D., Adames, Á. F. & Sukhatme, J. WISHE-Moisture Mode in an Aquaplanet Simulation. J. Adv. Model. Earth Syst. 10, 2393–2407 (2018).

65.

Singh, B. & Kinter, J. L. Tracking of Tropical Intraseasonal Convective Anomalies: 1. Seasonality of the Tropical Intraseasonal Oscillations. J. Geophys. Res. Atmos. 125, (2020).

66.

Sobel, A. & Maloney, E. An Idealized Semi-Empirical Framework for Modeling the Madden–Julian Oscillation. Journal of the Atmospheric Sciences 69, 1691–1705 (2012).

67.

Sobel, A. & Maloney, E. Moisture Modes and the Eastward Propagation of the MJO. Journal of the Atmospheric Sciences 70, 187–192 (2013).

68.

Straub, K. H. MJO Initiation in the Real-Time Multivariate MJO Index. Journal of Climate 26, 1130–1151 (2013).

69.

Wang, B., Chen, G. & Liu, F. Diversity of the Madden-Julian Oscillation. Sci. Adv. 5, eaax0220 (2019).

70.

Wang, B. & Lee, S.-S. MJO Propagation Shaped by Zonal Asymmetric Structures: Results from 24 GCM Simulations. Journal of Climate 30, 7933–7952 (2017).

71.

Wang, B. et al. Dynamics-oriented diagnostics for the Madden-Julian Oscillation. J. Climate JCLI-D-17-0332.1 (2018) doi:10.1175/JCLI-D-17-0332.1.

72.

Wheeler, M. C. & Hendon, H. H. An All-Season Real-Time Multivariate MJO Index: Development of an Index for Monitoring and Prediction. Mon. Wea. Rev. 132, 1917–1932 (2004).

73.

Wheeler, M. & Kiladis, G. N. Convectively Coupled Equatorial Waves: Analysis of Clouds and Temperature in the Wavenumber–Frequency Domain. J. Atmos. Sci. 56, 374–399 (1999).

74.

Wolding, B. O. & Maloney, E. D. Objective Diagnostics and the Madden–Julian Oscillation. Part II: Application to Moist Static Energy and Moisture Budgets. Journal of Climate 28, 7786–7808 (2015).

75.

Wu, C.-H. & Hsu, H.-H. Topographic Influence on the MJO in the Maritime Continent. Journal of Climate 22, 5433–5448 (2009).

76.

Zhang, C. Madden-Julian Oscillation: MADDEN-JULIAN OSCILLATION. Rev. Geophys. 43, (2005).

77.

Zhang, C. & Ling, J. Barrier Effect of the Indo-Pacific Maritime Continent on the MJO: Perspectives from Tracking MJO Precipitation. J. Climate 30, 3439–3459 (2017).

78.

Zhou, S., L'Heureux, M., Weaver, S. & Kumar, A. A composite study of the MJO influence on the surface air temperature and precipitation over the Continental United States. Clim Dyn 38, 1459–1471 (2012).